DEVELOPMENT OF A
LOW ENERGY ION MASS SPECTROMETER

By

SPYRIDON KARAPETSAS, B.Eng.

A Project Report
Submitted to the School of Graduate Studies
in Partial Fulfilment of the Requirements
for the Degree
Master of Engineering
McMaster University
February, 1982

MASTER OF ENGINEERING (1982) (Engineering Physics)	McMaster University Hamilton, Ontario

TITLE:	Development of a Low Energy Ion Mass Spectrometer
AUTHOR:	Spyridon Karapetsas, B.Eng. (McMaster University)
SUPERVISOR:	Dr. J.E. Robinson
NUMBER OF PAGES:	X, 86

ACKNOWLEDGEMENTS

I would like to thank Dr. J.E. Robinson for his guidance during the course of this project and Dr. D.A. Thompson for his critical review and helpful comments on the manuscript. I thank the National Research Council for the Postgraduate Scholarship award and McMaster University for the Teaching Assistantship award. I also wish to thank the Engineering Machine Shop personnel for assisting me with the design of the mechanical assemblies and Mr. G. Leinweber for constructing the electronic assemblies.

ABSTRACT

The interaction mechanisms of an ion beam with a solid target are identified. Basic parameters associated with ion scattering, charge neutralization, inelastic energy losses and secondary ion production are described. Low energy (1-20 kev) experimental studies on these topics are reviewed. A low energy ion mass spectrometer is described. The ion beam is generated by an existing kev ion accelerator and is directed to a newly constructed UHV target chamer. The energy and angular distributions of the backscattered particles are measured with a hemisperical electrostatic analyser and a channeltron detector. A high precision goniometer allows target rotation about two perpendicular axes by angles of 180^{o} and 90^{o} with an accuracy and repeatability of 0.1^{o}. The interaction chamber is bakeable to $250^{o}C$ and was designed for an ultimate pressure of 10^{-11} torr. The data acquisition system chamber scans the energy spectrum automatically so that the radiation dosage at the target is equalized for all channels.

TABLE OF CONTENTS

LIST OF ILLUSTRATIONS

CHAPTER 1

INTRODUCTION

Many recent technological advances can be attributed to ingenious applications of our knowledge about basic phenomena and processes occuring at material interfaces. The development of the modern computer is a good case in point. Since the invention of the transistor in 1948, the speed and size of computing machines has been totally controlled by advances in the technology of thin films. Also, future breakthroughs in such areas of technology as energy production, corrosion prevention, adhesive coatings, catalysis and lubrication are conditionally dependent on further advances in surface science. This is the scientific body of knowledge concerning the properties of the vacuum to solid interface.

In a report to the American Physical Society (1), a special study group on physics problems relating to energy technology, pointed out that studies in the following surface processes are of paramount importance in the design and construction of Controlled Thermonuclear Reactors (CTR):

(1) the reflection of particles and energy back into plasma
(2) charge exchange of plasma particles at the wall
(3) secondary electron and photon production
(4) defects and foreign atoms introduced into the wall
(5) contamination of the plasma by desorption of adsorbed species, sputtering of wall material, blister material and exfoliation of wall material.

Before proceeding any further we must first define what is meant by 'surface' and explain how certain surface properties are being investigated.

According to Park (2), 'the surface region of a solid may be defined as the layer in which the atomic potentials differ from those of atoms still deeper within the solid'. Included in this definition are atoms with broken bonds 'dangling' in the vacuum as well as atoms within the solid sensing the effects of these bonds. Such a surface is normally characterized as 'atomically clean'. However, of particular interest to material science are 'practical surfaces'. Fig. 1.1 is a schematic of a planar cut into a crystalline solid showing a practical surface. The figure illustrates that a surface usually contains foreign atoms and molecules which are either adsorbed at the surface or absorbed in an intermediate region of the solid called 'the selvedge' (3). According to Hagstrum (4), 'the atomic traffic in both directions between surface and selvedge is very important in surface studies'.

Surface characterization involves determining the chemical identity of the constituent atoms, their geometrical arrangement and the spatial and energy distribution of their electrons. Information on surfaces is normally obtained by inducing these atoms to emit characteristic radiation. Figure 1.2 indicates all the possible combinations of incident/emitted radiations which can be utilized in the study of surfaces. The following is a list of the various surface characterization techniques:

Ion spectroscopy
Electron spectroscopy
Photoemission spectroscopy
Molecular spectroscopy
Field spectroscopy

The underlying processes yielding the information carrying radiation is different in each of these spectros-

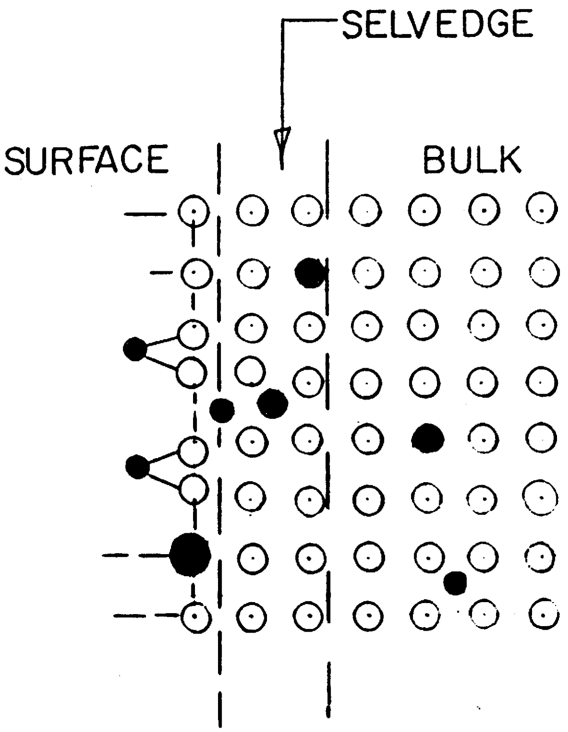

Fig. 1.1 Planar cut of a crystal indicating a. surface b. selvedge c. bulk.

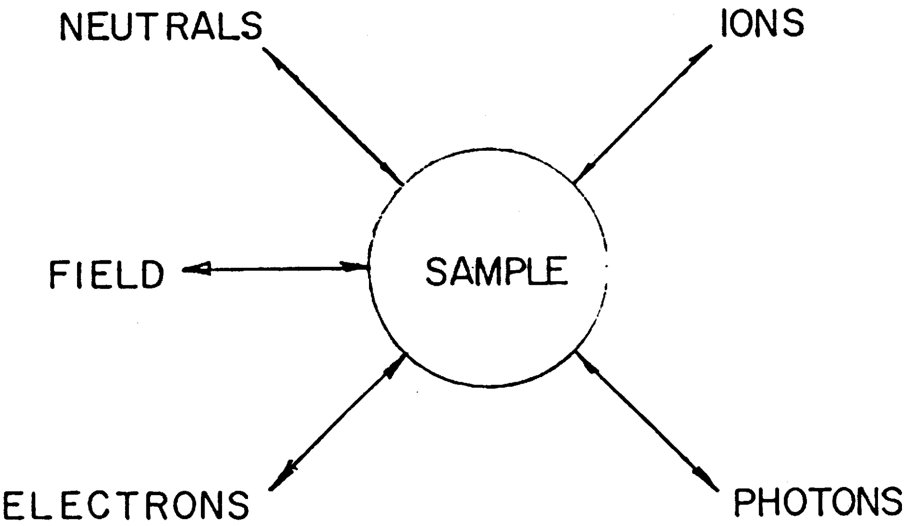

Fig. 1.2 Possible types of input/output radiation used for surface analysis.

copies. For example, Low Energy Ion Spectroscopy (LEIS) depends on two processes: (a) elastic backscattering of ions and (b) escape from neutralization. On the other hand, Auger Electron Spectroscopy (AES) relies on core-hole recombinations leading to Auger electron emission. Consequently, each technique used in isolation has it's inherent limitations with respect to signal sensitivity, mass resolution, sampling depth and the capability of providing quantitative and topographical surface information. This has lead many researchers (5,6,25) to extend the capabilities of their surface study instruments by incorporating a combination of these techniques in the same experimental apparatus.

The objective of this project was to extend the capabilities of an existing LEIS by providing the instrumentation for the electrostatic analysis of backscattered ions. This involved constructing a new target chamber, a high precision goniometer and the support assembly for the detection system which consisted of a hemispherical condenser and a channeltron detector. Also an automatic data acquisition system was constructed with the capability to monitor the beam current at the target. This allowed control of the Multichannel Analyser dwell time in a manner which equalized the radiation dosage for all channels.

A Time-of-Flight (TOF) port on the vacuum chamber made the system compatible with an existing experimental set up. Also, an Auger port made allowance for future expansion.

CHAPTER 2

THEORY

2.1 Physical Processes

Consider a well collimated and monoenergetic ion beam incident normally on a solid target. After interacting with target atoms, the beam particles may be classified into two groups: (1) backscattered and (2) trapped. Figure 2.1 illustrates representative trajectories of particles which were reflected because of surface scattering and single or multiple collisions within the target. Figure 2.2 does the same for particles belonging to the second group.

It is relatively easy to derive the physics for surface scattering. Conservation of energy and momentum parallel and perpendicular to the direction of incidence yields

$$\frac{1}{2}M_1Vo^2 = \frac{1}{2}M_1V_1^2 + \frac{1}{2}M_2V_2^2 \qquad (2.1)$$

$$M_1Vo = M_1V_1\mathrm{Cos}\theta + M_2V_2\,\mathrm{Cos}\varphi \qquad (2.2)$$

$$0 = M_1V_1\mathrm{Sin}\theta - M_2V_2\,\mathrm{Sin}\varphi \qquad (2.3)$$

where,

θ and φ are the angles of the primary and target atoms in the laboratory system with respect to the direction of incidence after the collision event.

$Eo = 1/2\ M_1V_o^2$ is the energy of incidence, $E_1 = 1/2M_1V_1^2$ is the energy of reflection and $E_2 = 1/2M_2V_2^2$ is the energy of recoil.

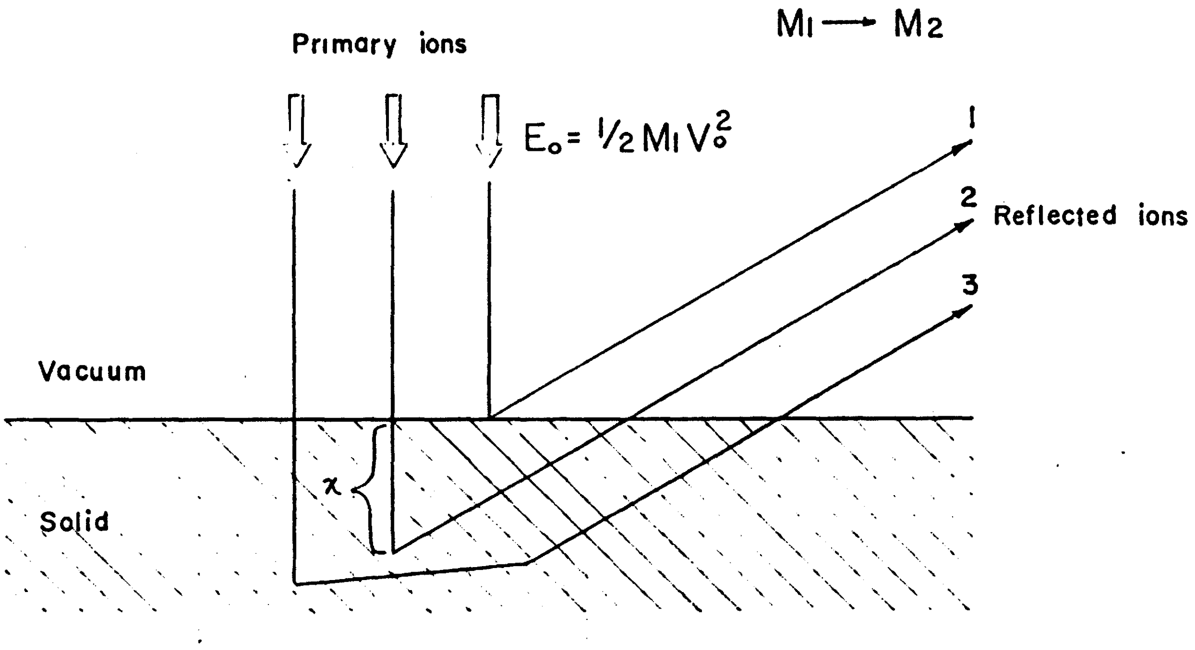

Fig. 2.1 Representative trajectories of reflected ions.

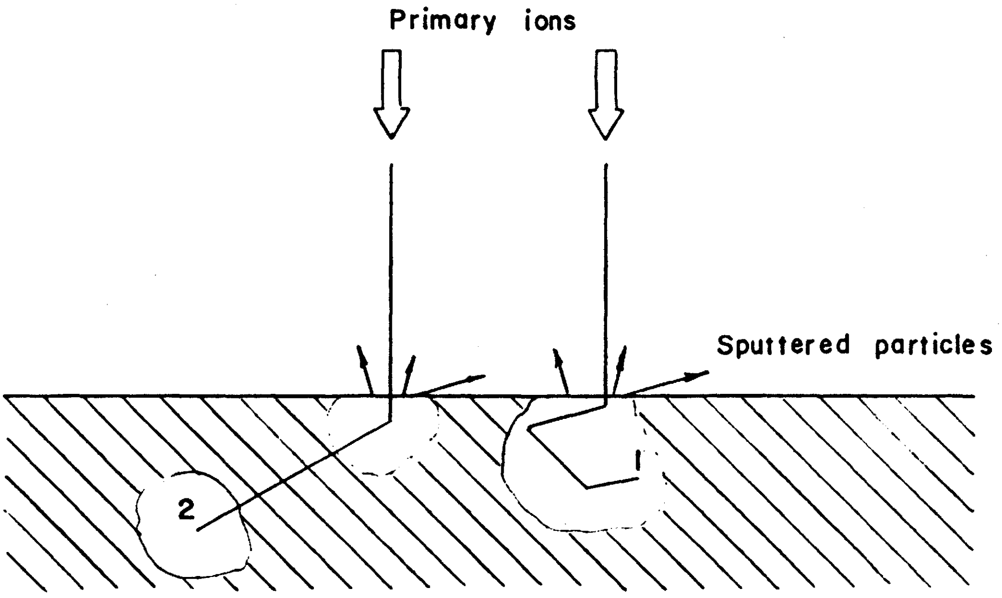

Fig. 2.2 Representative trajectories of trapped ions.

Eliminating V_2 from these equations, we obtain

$$\frac{V_1}{V_o} = \left[\pm(M_1{}^2-M_1{}^2\text{Sin}^2\theta)^{1/2} + M_1\text{Cos}\varphi\right] \Big/ (M_2+M_1) \qquad (2.4)$$

or

$$E_1 = KE_o \qquad (2.5)$$

where

$$K = \left[(M_2{}^2-M_1{}^2\text{Sin}^2\theta)^{1/2} + M_1\text{Cos}\theta \Big/ (M_1+M_2)\right]^2 \qquad (2.6)$$

Hence, assuming that the interaction event was an elastic binary collision, eg. 2.5 establishes that the energy of the backscattered particle carries information about the mass of the scatterer. The factor K is normally called the kinematic factor.

The second particle in Figure 2.1 is shown to penetrate a distance X into the solid before colliding with a substrate atom and subsequently being reflected into vacuum. As it moves through the solid, it loses energy by electronic excitation at a rate proportional to the stopping power of the material. Hence, it's energy at depth X is given by

$$E(x) = Eo - \int_o^x \left(\frac{dE}{dX}\right) d\,X' \qquad (2.7)$$

After the atomic collision of depth X, the energy of the particle is given by equation 2.5.

Consequently the energy of reflection can be calculated by taking into account both elastic and inelastic energy losses as follows:

$$E_1' = E_o - K\int_o^x \left(\frac{dE}{dx}\right)_{Eo} dx' - \int_{x/\text{Cos}\theta}^{o} \left(\frac{dE}{dx}\right)_{KEo} dx \qquad (2.8)$$

Although difficult to express analytically, ion backscattering involving multiple collisions within a target is simply an extension of the previous event. In general, the following equation holds true.

$$E_1 = Eo - Ea - Ee \tag{2.9}$$

where,

Ea is the total energy transferred to target atoms due to elastic collisions,

and

Ee is the total energy loss due to inelastic processes.

Considering the case of double coplanar backscattering (particle 3, Figure 2.1) so that $\theta=\theta_1+\theta_2$, this results in the minimum energy transferred to the target and for small depths of penetration, the energy of the reflected particle from within the solid is greater than the energy of a surface scattered particle.

Despite the fact that particle number 1 in Figure 2.2 ends up being trapped after dissipating all of its energy within the solid, some particles are still ejected into vacuum. These are target atoms which receive sufficient energy and momentum to escape the surface barrier. The phenomenon is called sputtering and is caused by a series of correlated collisions of target atoms initiated by the incident ion.

The particles which are ejected from the target may emerge as either neutral or charged. If we represent by R(E) the energy spectrum of the reflected primaries, S(E) the energy distribution of the sputtered secondaries, and $I^+(E)$ the probability that an emerging particle of energy E will be singly and positively ionized then

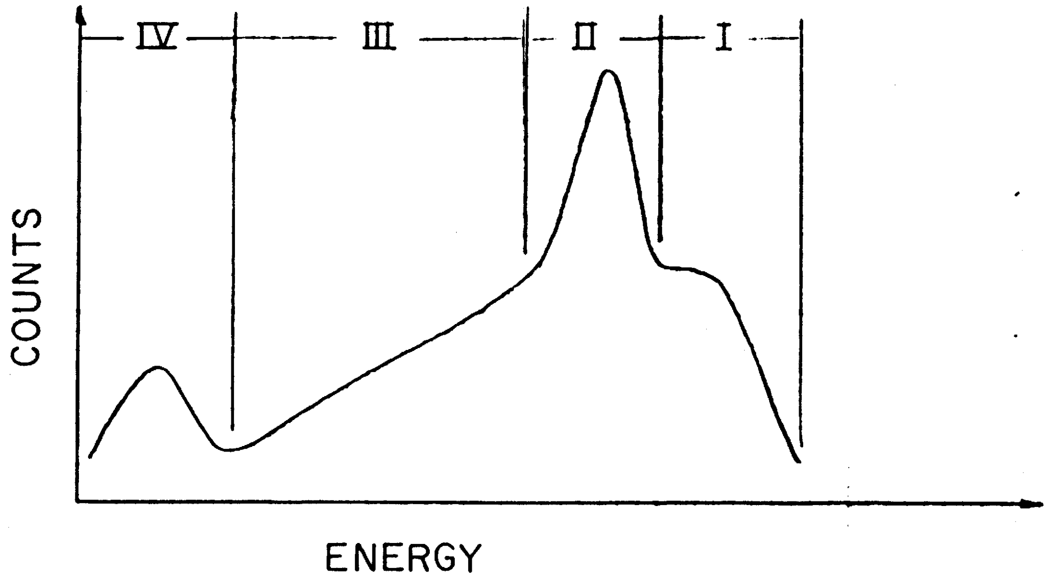

Fig. 2.3 Typical low energy noble gas backscattering ion spectrum.

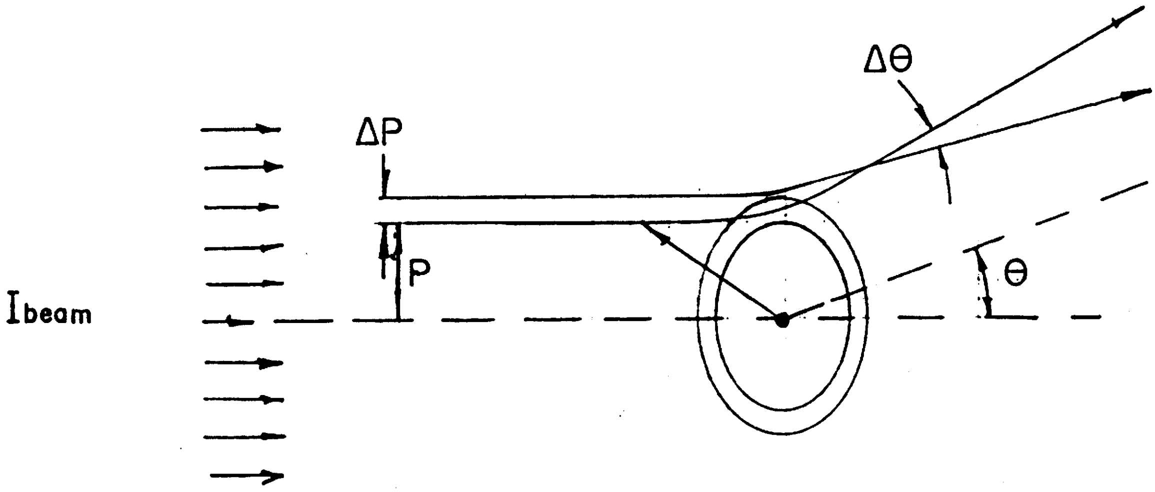

Fig. 2.4 The differential cross section represents an area around the atom which when struck by incident ion results in an angle of reflection between θ and θ + dθ.

$$N^{+}(E) = R(E)I_1^{+}(E) + S(E)I_2^{+}(E) \qquad (2.10)$$

represents the energy spectrum of the positive ions ejected from the target as a result of the ion beam bombardment.

Figure 2.3 is such a spectrum generated by a low energy (1-15 Kev) noble gas ion beam. There are four features in it which can be directly attributed to the interaction processes described so far. The most predominant feature is the surface peak in region II. The position and height of this peak is determined by the chemical composition and relative abundance of the scattering centers on the target surface. Double scattering events contribute to the shoulder on the high energy end of the spectrum (region I). The rapid fall off in the intensity of the ion backscattering signal observed in region III is due to preferential neutralization of particles penetrating into the target and losing most of their energy in multiple collisions. Sputtered target ions accounts for the peak observed at the low energy end. (region IV).

2.2 Theoretical Considerations

This section review important theoretical aspects concerning the various ion-matter interaction processes. When no underlying theoretical basis exists, the treatment is qualitative in nature and those phenomena which are of current scientific interest are pointed out.

2.2.1 The Kenematic Factor K

The kinematic factor K in equation 2.5 provides a unique relation between the mass of a scatterer and the energy of the reflected primary particles. This fundamental expression establishes backscattering spectroscopy as a tool for the elemental analysis of surfaces. The purpose of this section is to examine the sensitivity of the technique with respect to the following three experimental parameters:

(a) angle of reflection
(b) mass of the ion probe
(c) energy of incidence

Consider the change ΔE in the backscattering energy caused by a change ΔM_2 in the mass of the target atoms, it follows from eg. 2.5 that ΔE can be expressed by:

$$\Delta E = Eo \left(\frac{dK}{dM_2} \right) \Delta M_2 \qquad (2.11)$$

Utilizing the following equation between K and the scattering angle θc in the center-of-mass coordinate system:

$$K = 1 - \frac{2M_1M_2 \quad (1-\text{Cos}\theta c)}{(M_1+M_2)} \qquad (2.12)$$

we obtain:

$$\frac{dK}{dM_2} = \frac{2M_1(M_2-M_1) \ (1-\text{Cos}\theta c)}{(M_1+M_2)^2} \qquad (2.13)$$

and for $\frac{M_2}{M_1} \gg 1$

$$\frac{dK}{dM_2} \simeq 2\frac{M_1 \ (1-\text{Cos}\theta c)}{M_2}$$

Since for values of θc between 90° and 180° dK/dM_2 increases monotonically, eg. 2.11 indicates that the maximum energy separation between the surface peak of two different atomic species is attained by observing the target at an angle as close to 180° as other experimental constraints permit. This equation also indicates that the mass resolution is inherently better for lighter atoms and it can be improved by using heavier ions. About the dependence on the energy of incidence, eg. 2.11 states that the mass resolution is higher for more energetic beams. However, this is a secondary effect since the ion backscattering signal to noise ratio is improved considerably at low energies (1-5kev) because of an increase to the probability of neutralization. This subject is discussed in a subsequent section.

2.2.2 The Differential Cross Section

The quantitative interpretation of backscattering energy spectra requires knowledge of how the differential cross section d_6 depends on the energy of the incident ions and the identity of the target atoms. This quantity represents the geometrical area of an atom such that if it is struck by an ion of energy E, it will be scattered by an angle between Θ and $\Theta+d\Theta$ (fig. 2.4). Depending on the parameter which is experimentally important, d_6 can be expressed as a function of either the transfer energy T, or the solid angle Ω according to the following two equations.

$$d_6 = \frac{d6}{dT} \, dT \qquad (2.15)$$

$$d_6 = \frac{d_6}{d\Omega} \, d\Omega \qquad (2.16)$$

The first expression is useful in radiation damage studies. However, whenever scattering is observed with a detector, the second equation is more convenient to use.

As an example of how experimental data on cross sections can be used for the compositional analysis of a solid, consider the energy spectrum of Figure 2.5. It is apparant from the position of the surface peaks that the target is a compound of Ga and P. Furthermore, by dividing the area of these peaks by the total cross ection for each element the composition of the material was found to be $GaP_{1.o}$ which is stoichiometric.

$$\frac{N_{Ga}}{Np} = \frac{\text{No. of Ga atoms}}{\text{No. of P atoms}} = \frac{6e}{6Ga} \cdot \frac{HGa}{Hp} \qquad (2.17)$$

where, HGa and Hp are the peak heights for Ga and P respectively.

In radiation damage studies the differential cross section is used for averaging. For example, if an analytical expression was available for d_6 then it would be possible to calculate such parameters as the stopping cross section S(E), the mean transferred energy $\langle T_2 \rangle$, and the average deposited energy per unit length T_L as shown by the following equations.

$$S(E) = \int_o^{T_M} Td6 \qquad (2.18)$$

$$\langle T_2 \rangle = \frac{\int_o^{T_M} T_2 \, d6}{\int_o^{\infty} d6} \qquad (2.19)$$

$$T_1 = \frac{\langle T2 \rangle}{L} = \frac{\langle T2 \rangle}{\frac{1}{6N}} \qquad (2.20)$$

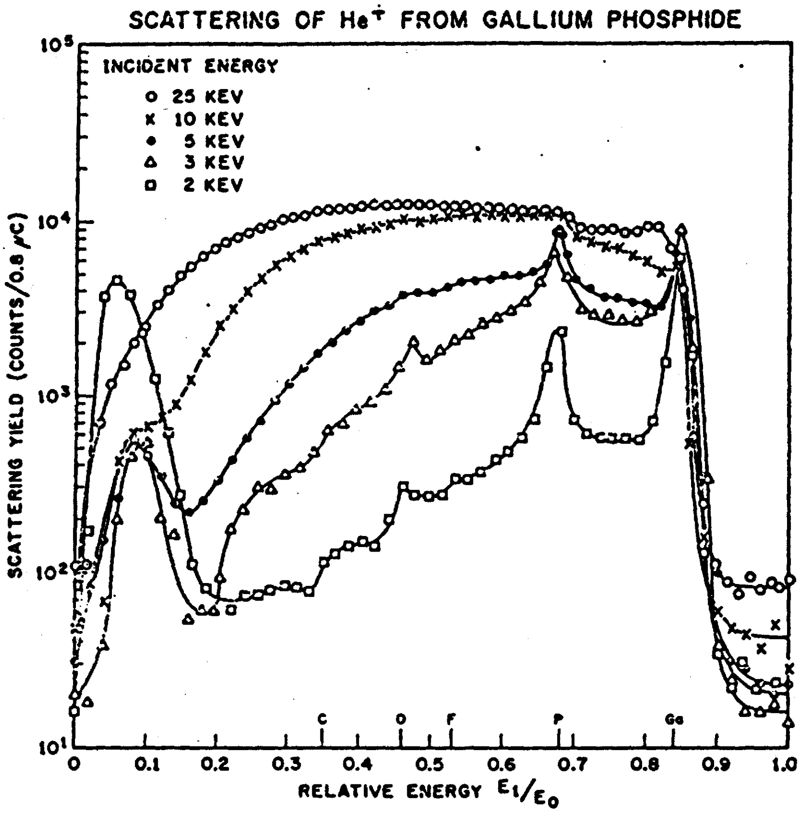

Fig. 2.5 Scattering yield of He^+ from GaP (Ref.20).

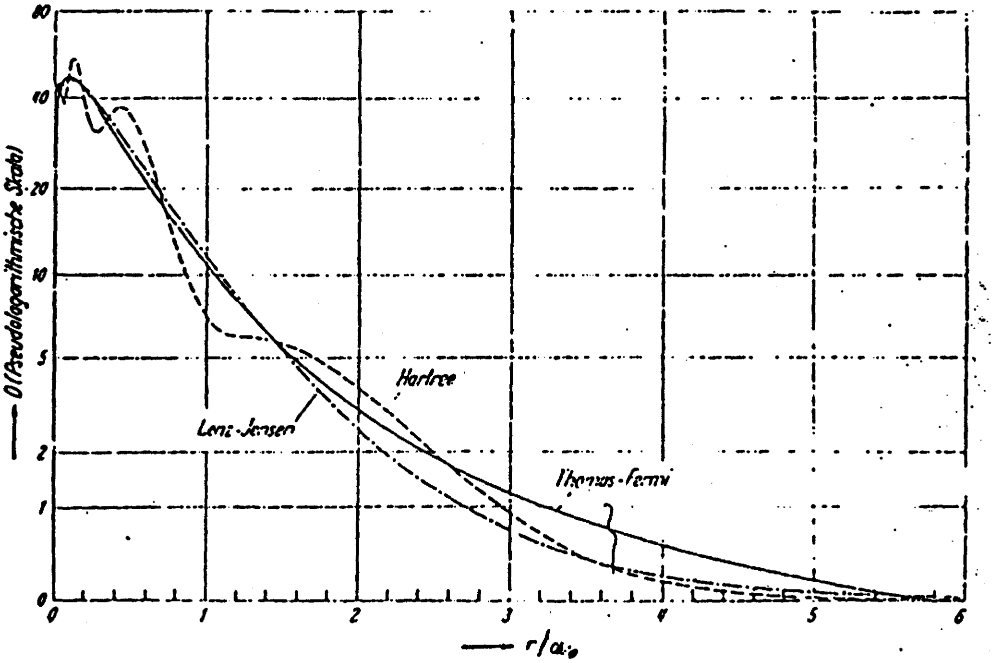

Fig. 2.6 A comparison between three different interatomic potentials.

The dependence of $d\sigma$ on energy and ion-atom combination is determined primarily by the assumed form of the interaction potential V (r) between the colliding particles. V(r) arises from the many body electronic interactions between the nuclei and their orbiting electrons. In general, V(r) is made up of three terms: a nuclear repulsion term Enn, an electronic repulsion term Eee and finally the electron nuclei attraction term Een. At low energies, the colliding particles come close enough for their electronic shells to overlap, yet they are still sufficiently apart for a direct interaction between the bare nuclear charges. In this case V(r) can be represented by eq.2.22. This is a screened coulomb potential with φ, being the electronic screening function normalized to atomic distance units by the first Bohr radius a_o.

$$V(r) = Enn + Eee + Een \tag{2.21}$$

$$V(r) = \frac{Z_1 Z_2 e^2}{4\pi \epsilon_o r} \varphi (r/a) \tag{2.22}$$

where, Z_1 and Z_2 are the atomic numbers of the particles, e is the electronic charge and ϵ_o is the dielectric constant for vacuum.

Although many analytical expressions have been proposed for φ none of them is universal. Their range of validity is determined by the mass and energy of the incident ions. For light projectiles and for collision events resulting in distances of closest approach from $.5a_o$ to $10a_o$ the Thomas-Fermi potential is a good approximation for V(r). This potential is based on the Thomas-Fermi statistical model of an atom, Figure 2.6 compares the T-F to a Hartee-Fock potential based on a more accurate quantum-mechanical treatment of the interaction problem. Firsov (7) represented $V_{TF}(r)$ as

$$V_{TF}(r) = \frac{Z_1 \; Z_2 e^2}{r} \; x(\Psi(Z_1, Z_2)\frac{r}{a})$$

where,

$X(x)$ is the T-F screening function

$a=(9\pi^2/128)^{1/3}\hbar^2/me^2=4.7\cdot10^{-9}\text{cm}$

$\Psi(Z_1,Z_2)=(Z_1^{2/3} + Z_2^{2/3})^{1/2}$ for $2<x<7$

$\Psi(Z_1,Z_2)=3 \left[(Z_1+Z_2)^{7/3}-Z_1^{7/3}-Z_2^{7/3})\right] 7Z_1Z_2$

for $0<x<2$

Lindhard et al.(8) derived the following approximation to the T-F differential cross section.

$$d_6 = \pi a^2 \frac{dt}{2t^{3/2}} f(t^{1/2}) \tag{2.24}$$

where,

$t = \epsilon^2 \; T/Tm$

$Tm = \gamma E$

E = energy of incidence

T = recoil energy

$\gamma = 4M_1M_2(M_1+ M_2)^2$

M_1 = mass of scattered particle

M_2 = mass of recoiling particle

$\epsilon = \left(\frac{M_2E}{M_1M_2}\right)\left(\frac{Z_1 \quad Z_2e^2}{a}\right)^{-1}$

Z_1 = atomic number of incident particle

Z_2 = atomic number of recoiling particle

$a = 0.8853 \; a_o Z^{-1/3}$

$Z^{2/3} = Z_1^{2/3} + Z_2^{2/3}$

$a_o = 0.529\text{Å}$

and

$f(t^{\frac{1}{2}})$ is a function determined by numerical methods

$$f(t^{\frac{1}{2}}) = (1.309)\ t^{1/6} \left[1 + (2.618\ t^{2/3})^{2/3}\right]^{-3/2}$$

2.2.3 Charge Neutralization

An energetic ion moving inside a solid carries potential energy by virtue of the fact that it is ionized. During an atomic collision, it is possible that the ion may give off some or all of this potential energy by capturing one or more electrons from the target material. The inverse process, further ionization by electron stripping, is also possible but is is less likely to occur.

Data on charge neutralization for various materials are of intense interest to fundamental research as the nature of the charge exchange mechanism is still not well understood. They are also useful in many practical areas including low energy ion backscattering, spectroscopy and the design of magnetic confinement thermonuclear devices.

Three basic neutralization mechanisms have been proposed so far: (a) resonance tunneling, (b) Auger and (c) radiative neutralization. Resonance tunneling is the process in which an electron from a level in the solid below the Fermi level moves into an excited level at the same energy in the ion. The reverse process, resonance excitation, is also possible and is indicated by the solid arrow in Figure 2.7. Auger neutralization involves two electrons: one tunneling into the ground state of the ion, while the second one is simultaneously being ejected with the same amount of energy of the first transistion (Figure 2.8). If the atom emits a photon to compensate for the change in it's potential energy, then the process is called radiative neutralization.

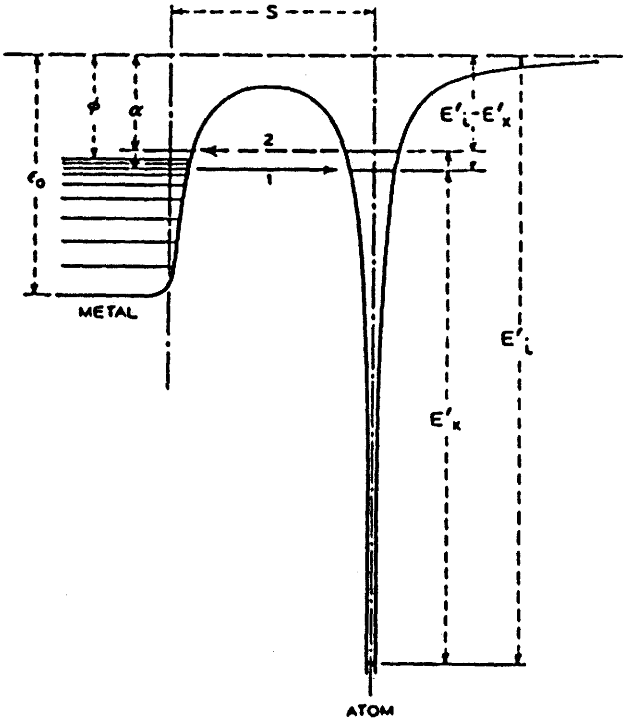

Fig. 2.7 Resonance tunneling (Ref.9)

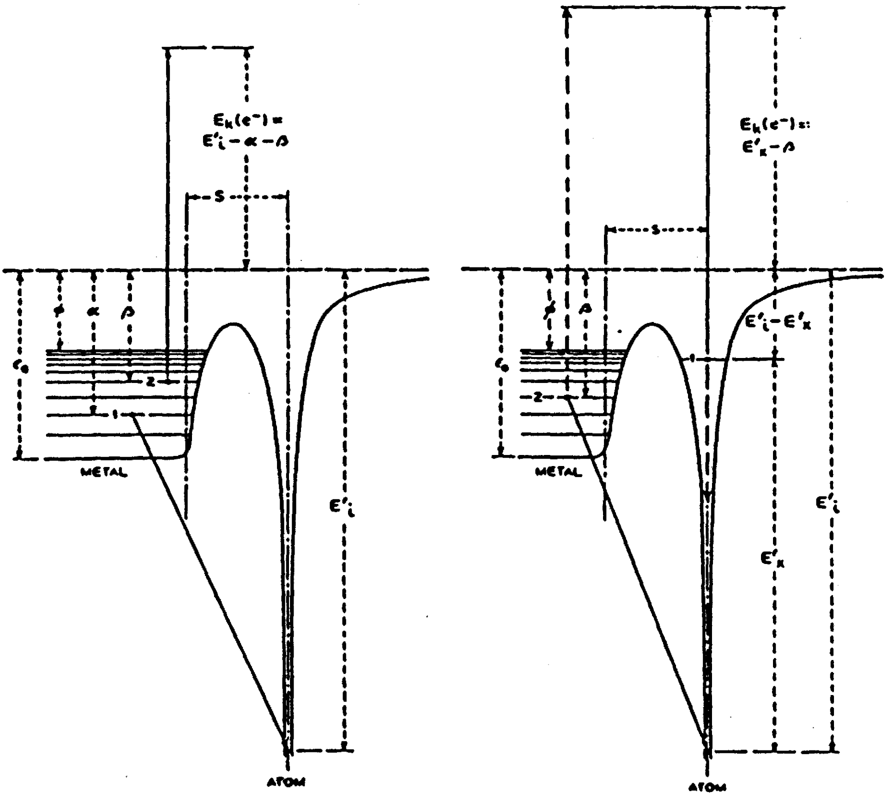

Fig. 2.8 Auger neutralization and de-excitation (Ref.9).

Each of these processes may be described in terms of probability functions expressing the likelihood that an ion will either return to it's ground state or will undergo a given electronic transition after travelling a distance X in a solid. In general it has been found that neutralization due to any single process decreases exponentially with increasing ion velocity according to equation 2.25.

$$Pi = A\exp(-\alpha/V_1) \qquad (2.25)$$

where,

V_1 is the ion velocity perpendicular to the target surface and α is a material constant.

This behaviour in Pi has been observed with many metals in the high energy regime. However, at low energies ($<$5kev) and with certain ion-target atom combinations the ion yield has been found to exhibit a fine oscillatory structure (Figure 2.9). Smith et al.(10) has proposed a resonant and quasi-resonant charge transfer mechanism to explain the variation in the neutralization proability. In essence, his model assumes the formation of a quasi-molecular state between the ion and the target atom. This occurs only when the velocity of a valence electron is of the same order as the ion velocity and the difference in the electronic potential between the original and final ion states is small. Under these conditions, the neutralization probability decreases as the electron can be transferred many times back and forth between the atom and the ion.

A controversial research topic concerns the distance from the surface where neutralization takes place.

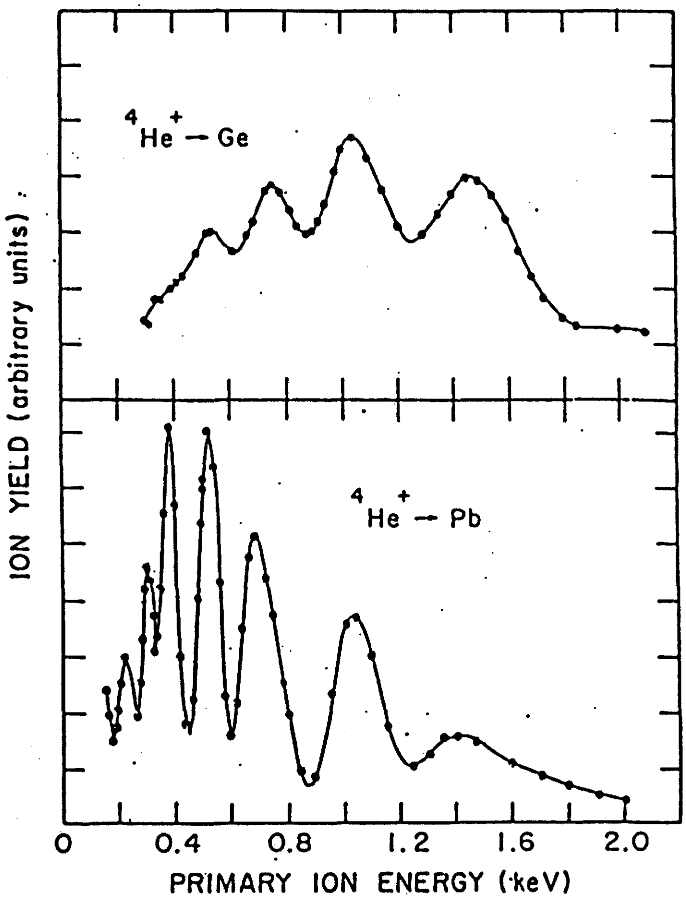

Fig. 2.9 Scattered ion yield curves for He^+ illustrating the oscillatory nature of the ionization probability for certain elements (Ref. 10).

Two contradictory theories have been put forward. The first one assumes that a Debye-type screening by the electron gas prevents the formation of bound states of the ion inside a metal target, thus concluding that the charge transfer must occur just outside the surface. The second one allows neutralization to occur inside the solid and in fact attributes the extreme surface sensitivity of LEIS to preferential neutralization of the ions penetrating below the top few atom monolayers.

More theoretical and experimental work is necessary in order to establish a clear picture of the charge exchange processes between an energetic ion and a solid.

2.2.4 Inelastic Energy Losses

It is obvious from the previous section that the electron interaction of an ion travelling inside a solid is a rather complicated phenomenon involving many processes. Consequently, an exact analytical description of how the various interaction mechanisms degrade the energy of the ion is a very difficult task. A degree of simplification results by averaging all modes of inelastic energy loss into a single parameter called the electronic stopping power of the material Se.

In a quasi-classical treatment of the electronic interaction, Firsov(11) derived an expression for Se by considering the momentum transfer resulting from the movement of bound electrons into the potential field of the moving ion. He found that Se is given by equation:

$$Se = \frac{0.35(Z_1+Z_2)^{5/3}\hbar V/ao}{\left[1+0.16(Z_1+Z_2)^{1/3}\ Ro/a_o\right]^5} \qquad (2.26)$$

where,

Z_1, Z_2 = is the atomic number of the target and projectile atoms.

a_o = is the first Bohr radius

R_o = is the impact parameter

This equation assumes a Thomas-Fermi interaction potential and is applicable to small scattering angles.

Another approximation of Se is by Lindhard and Scharff(58). They found that at ion velocities small by comparison to V^1 where, $V^1 = Z^{2/3}$ Vo and Vo is the velocity of an electron in the first Bohr orbit, Se is given by

$$Se = \xi 8\pi e^2 a_o (Z_1 Z_2 / Z) \; V/vo \qquad (2.27)$$

where,

ξ is of the order of 1 to 2

and

$Z = (Z_1^{2/3} + Z_2^{2/3})^{3/2}$

Both equations 2.26 and 2.27 show the same linear dependence of Se on the velocity of the ion. However, they differ in one important respect. Lindhard's approximation does not show any dependence of Se on the impact parameter.

The validity of the theoretical models used in the derivation of these expressions has been checked by a number of semiempirical simulation studies.

For example, Thomphson et al. (12) using a Monte Carlo computer simulation program, calculated the reflection coefficient of 10-40 kev proton on Si and by comparing it to experimental data, he concluded that Lindhard's approximation underestimates the electronic stopping power by approximately 60 %. In a similar study, Oen and Robinson (13) found that there is definitely a dependence of Se on the impact parameter as predicted by Firsov.

2.2.5 Secondary Ion Production

The phenonmenon of secondary ion production involves a combination of three processes: (a) energy dissipation of a primary particle within the target,

(b) sputtering of the target atoms located on the surface monolayer and (c) escape from neutralization. Two of these processes have already been dealt with. This section concentrates primarily on sputtering.

It is known from solid state physics that atoms are bound to the bulk of a solid with a certain amount of energy Ed called the displacement energy. If in a collision event, more energy than Ed is transferred to the struck lattice atom, then it can leave it's site and be set in motion. This event could be the beginning of a collision cascade when, according to Sigmund (14), the primary initiates a series of collisions whereby all the incident energy dissipates in a small volume. In case the direction of the collision cascade is towards the surface of the solid, then it is possible to transfer enough backward momentum and energy to the atoms of the top monolayer so that they can escape the surface barrier and sputter into vacuum.

Two quantities of interest in sputtering studies are the sputtering yield Ss and the Single Charged Ion (SCI) yield. Gries (15), using an expression for the number of recoils per incident ion taken from Sigmund's Random Collision Cascade Theory (16), derieved the following expression for the energy distribution of isotropically sputtered particles.

$$\frac{dN}{dE} = \frac{3}{2\pi^2} \alpha \frac{Sn(Ep)}{Co} \frac{E}{(E+B)^3} \qquad (2.28)$$

where α is a dimensionless parameter which depends on mass ration of bombarding element to the bombarded isotope, Sn(Ep) is the nuclear stopping cross section which is a function of the primary energy Ep, B is the surface binding energy and Co is equal to $1.81A^{o}$.

He also calculated the sputtered ion yeild S^+ assuming that $S^+ \propto N(E)R^+$ where R^+ is the ionization probability given by the following equation.

$$R^+ = \frac{B}{(I-W)} \cdot \left[\frac{h}{\Delta t(I-W)}\right]^n \qquad (2.29)$$

Hence,

$$S^+ = 0.231 \cdot \frac{S \cdot B^{5/2}}{\hat{\alpha} M^{1/2} (1-W)^3} \qquad (2.30)$$

In these equations I is the ionization energy of an atom with mass M, W is the electronic work function of the surface, B is the surface binding energy, $\Delta t - a/v$ is the time taken by a sputtered particle to go through the "thickness" a of the surface, $\hat{\alpha} = 2.9A^{o}$, S is Sigmund's sputtering coefficient and n is constant chosen to fit experimental results ($n \sim 1$). Figure 2.10 illustrates the general form of the sputtered ion spectrum required by equation 2.30.

Backscattered and sputtered particles carry away from the target a portion of the primary energy. Of the remaining available energy, another portion is lost due to electronic excitation and the balance goes into the creation of vacancies and interstetials. According to Sigmund's "Linear Cascade Theory" the number of vacancies created by low energy ion bombardment is a linerar function of the energy available for nuclear collisions. This theory is valid provided that collision cascades do not overlap in time and space.

In the case of molecular beam bombardment, the requirement of linearity appears to break down. An interaction mechanism called 'the thermal spike' has been

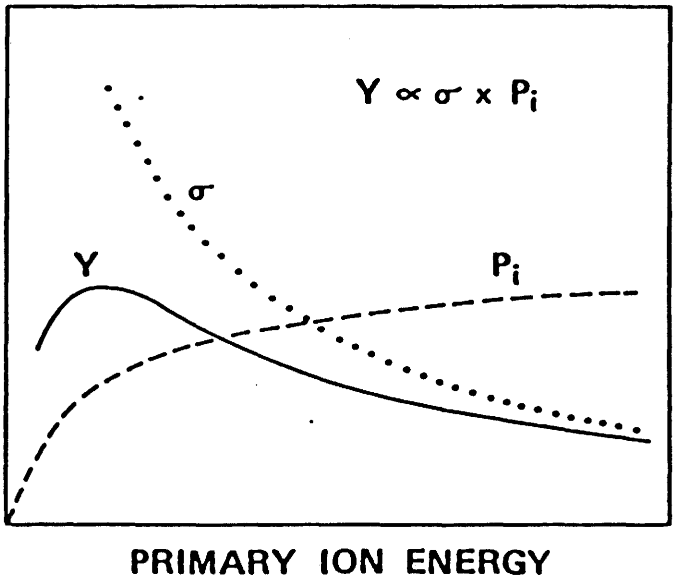

Fig. 2.10 Sputtered ion spectrum.

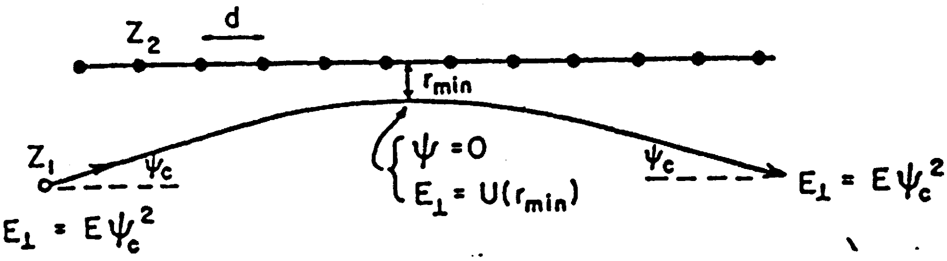

Fig. 2.11 The trajectory of a channeled beam (Ref.17).

proposed to account for the observed increase both in vacancy production and secondary ion generation. The thermal spike is associated with an effective reduction of the displacement energy to a few eV which indicates a material state close to melting.

2.2.6 Channeling

The material structure of a solid influences greatly the relative frequency of the various processes by which an energetic ion may interact with the solid. It has been found that if a well collimated ion beam strikes a crystalline target at an angle ψ to a low index axis, then provided that ψ is smaller than a certain critical angle ψ_c , the ions penetrating into the target get steered by successive gentle collisions with the atom rows into a path as the one shown in Figure 2.11. Consequently, they are prevented from having violent collisions with individual lattice atoms and lose their energy primarily by electronic excitation. This phenomenon is called channeling.

Channeling accounts for the observed drastic reduction in backscattering and sputtering yields. It is also responsible for a substantial increase in the projected range of the ions within the crystal and for an expected decrease in the amount of radiation damage introduced as vacancies.

Channeling effects have been observed at primary energies as low as 200ev and as high as 200 Mev. Similarly, projectiles as light as H and as heavy as Kr have been utilized for these experiments.

In the high energy regime ($E \sim$ MeV) Lindhard provided a theoretical description for channeling. He derived the following expression for the critical angle.

$$\psi_c = C \left[\frac{Z_1 Z_2 e^2}{dE}\right]^{1/2} \qquad (2.31)$$

where, E is the energy of the incident particle,

d is the atomic spacing and C is a constant between 1 and 2.

Low energy channeling is not well understood since it is sensitive to many factors which are difficult to control such a lattice temperature, surface contamination and beam divergence.

CHAPTER 3

REVIEW OF LITERATURE

3.1 Introduction

The following sections review the literature on (a) low energy ion beam surface characterization. (b) charge exchange mechanisms and (c) computer simulation studies of radiation damage of solids caused by ion bombardment.

3.1.1 Surface Characterization

Many experimental studies have been undertaken to establish LEIS as a quantitative surface analytical tool. The two major reasons motivating these studies is first the low construction cost of the necessary instrumentation and second, the relatively small destructive impact of low energy ion bombardment on the specimen under examination. A complete characterization of a surface requires elemental, compositional and structural analysis. In the following the experimental work on these topics will be reviewed.

In an early study (18) Smith proved that elastic binary collision theory was sufficient to describe atomic collisions in a solid to energies as low as 100ev. His investigation dispelled concerns about a possible increase in the 'effective mass' of atoms due to the cohesive forces of the solid. It appears that during the collision event, the atoms behave as if they are isolated from the solid. This, of course, simplifies considerably the interpretation of backscattering energy spectra since experimental values for the kinematic factor K may be regarded constant and independent of the primary energy.

The extreme surface sensitivity of low energy noble gas probes was demonstrated by a number of investigators.

(18,19,20,21,22,23). Smith accomplished this by monitoring the scattering signal from an atomically clean Mo surface exposed to CO. He observed that after cleaning the target, the intensity of the signal from Mo decreased for some time until it reached a steady state value. This coincided with the time required for the formation of a complete monolayer of CO on the surface. In a similar study (22), Buck reported that a single monolayer of Br gas can totally mask the signal from a Si substrate (Figure 3.1).

Ball et al.(20)investigated the shape of backscattering ion spectra obtained with inert gases as a function of the primary energy. He observed that as the energy was decreased, the height of the surface peak was also decreased. However, this was accompanied by a more rapid fall off of the ion yield at the low energy side of the spectrum with a considerable improvement in the signal to noise ratio (Figure 3.2). These effects were attributed to the preferential neutralization of the ions entering the solid bulk.

In the same study, the sensitivity of LEIS to trace impurities was measured by examination of precalibrated test samples and was found to be 5×10^{-4} monolayers of heavy elements such as gold and by extrapolation 10^{-1} to 10^{-2} monolayers for oxygen. All quantitative data were extracted from the spectra assuming a differential cross section based on a Born-Mayer potential.

The resolution of LEIS depends on the mass of the ion probe according to equation 2.11. Figure 3.3 taken from reference 19 verifies this relationship by illustrating that Ne^+ separates the surface peaks better than He^+. However, the gain in resolution must always be balanced against the loss in sensitivity since very heavy probes such as Xe^+ and Kr^+ are limited in their use by the fact that they do not backscatter from elements of lighter mass.

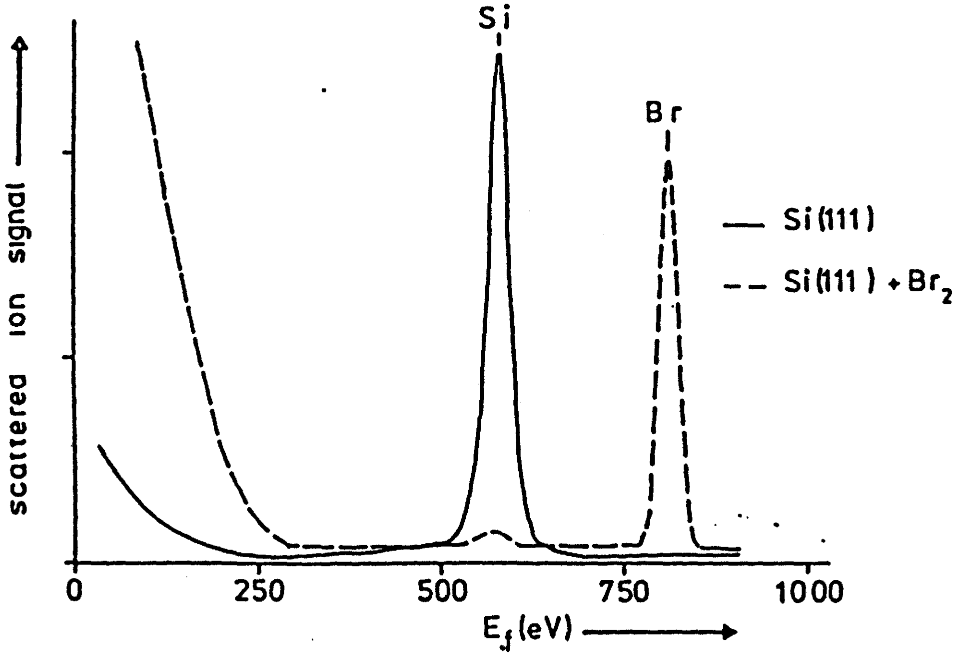

Fig. 3.1 An illustration of how a monolayer of Br can mask off the Si substrate (Ref.22).

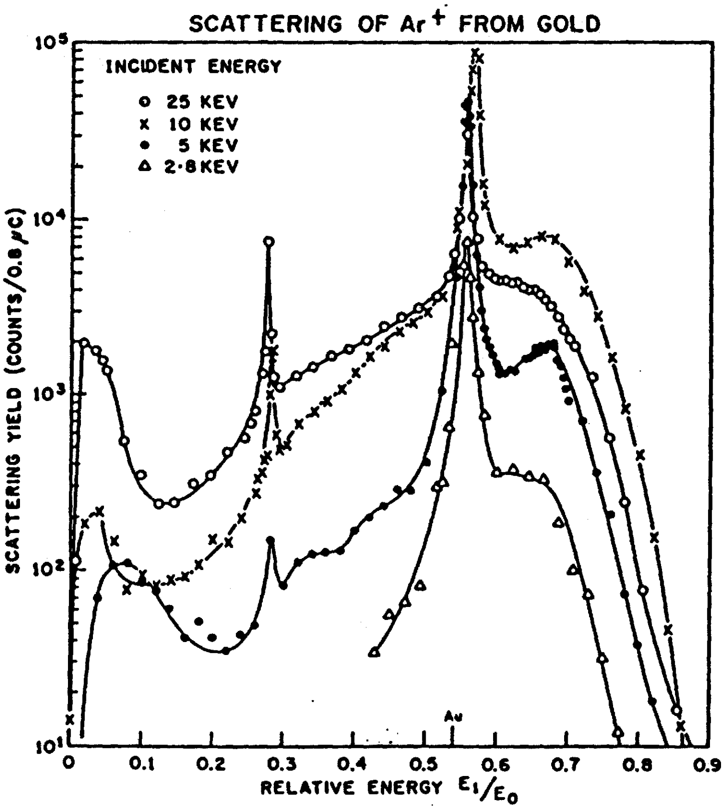

Fig. 3.2 This figure shows the dependence of backscattering Ar^+ spectra on the incident energy (Ref.20).

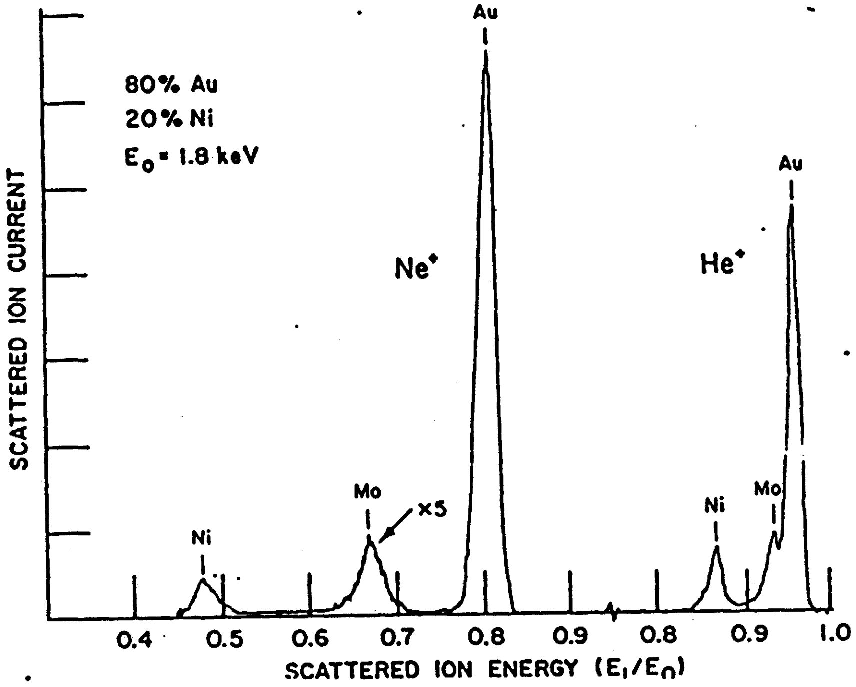

Fig. 3.3 The energy separation between surface peaks improves with heavier ion probes (Ref.19).

Since backscattering energy spectra contain information on the relative abundance of surface elements, LEIS has been used successfully for the compositional analysis of adsorbed gases (20,18,19) and for depth profiling of alloys (5,22). In the second application the spectra were obtained after successive removal of surface atom layers by Ar sputtering.

According to Park (2) a precise statement of surface composition must include the atomic arrangement (of the elements) because by contrast to homogenious bulk specimens a surface is inhomogeneous along its normal. H. Brongerman (21) utilized a secondary effect which he termed 'double sided shadow' to perform structural analysis of molecules adsorbed on a surface. He reasoned that an adsorbed molecule shields surface atoms from being directly hit by the incident ions and at the same time it prevents those ions which backscatter from the surface from reaching the detector. This effect modulates the scattering signal with spatial information. Beside adsorbed molecules, Brongerman employed LEIS to investigate the atom assignment of polar crystals (21,22).

3.1.2 Ion Neutralization Studies

There are three broad research areas which depend largely on charge neutralization data: LEIS, controlled fusion, and fundamental physics. First, if the ion escape probability was known for all materials and scattering angles, LEIS would become a quantitative and absolute analytical tool. Second, neutralization data on H, D and He ions are needed in evaluating the interaction of a hot plasma with the containment vessel walls of a d-t fusion reactor. In this case, the data is relevant to the plasma recycling problem which entails the neutralization of ions leaked through the magnetic confinement wall before they can be reintroduced back into the plasma.

Third neutralization data are also required in studies pursued by fundamental physics research aimed at broadening the knowledge on basic charge exchange mechanisms.

Neutralization probabilities have been studied as a function of the following parameters:

(a) emergent energy
(b) depth of penetration
(c) chemical composition of the bulk
(d) surface contamination

This section reviews the experimental findings on these topics.

H. Verbeek et al. investigated the interaction of low energy H ions with metal interfaces (24). He observed that the energy distribution of the neutrals has a pronounced maximum between 0.5 and 1.0 Kev whose position does not depend on the primary energy and angle of emergence. He also found that the charge fracetion $N^+/(N^+ + N^o)$ increases monotonically from approximately 3% at 300ev to 40% at 18 kev.

A totally different behaviour of the charge fraction has been observed for He, Ne and Ar ions (25,23). In these studies, Eckstein and Buck found that N^+/N_{TOT} plotted as a function of the backscattering energy contains distinct surface peaks. They concluded that inert and reactive gases must be subject to two different charge neutralization mechanisms. Furthermore, when Eckstein plotted his neutralization data for different incident He energies, he discovered that all the individual plots merged into a universal curve (Figure 3.4). He interpreted this as an indication that an equilibrium charge state was reached inside the bulk. However, Buck's similar data obtained for Ar at slightly higher energies are contradictory and they indicate preferential neutralization within the solid (Figure 3.5).

Eckstein also investigated the dependence of the inelastic energy losses on the velocity of the primaries. He did this by calculating the amount Q by which the surface peak in the positive spectrum is shifted to lower energies with respect to the energy of the single elastic collision. As expected, he found that energy losses dues to electronic excitation are linerearly related to the velocity of the primary. (Figures 3,6, 3.7).

Erickson and Smith (10,26) discovered an oscillatory dependence on the neutralization amplitude for certain ion-target combinations. This phenomenon was observed in the energy range .2 to 2 kev with elements having a d electron energy level which is approximately within 10ev of the first ionization energy of the incident ion. As described in a previous section, they explained these results by proposing a neutralization mechanism involving the formation of a quasi-colecular state while the ion is in close proximity with a target atom.

Eckstein and Verbeek have found early in the work (27), the influence of surface contamination on ion neutralization. Figure 3.8 taken from this study illustrates how a Nb surface cleaned by high temperature heating produces a sharp drop off in the high energy end of the backscattering energy spectrum. This was attributed to surface scattering. Surface contamination was responsible for the broadening of the spectrum shown by the lower curve. This experiment and

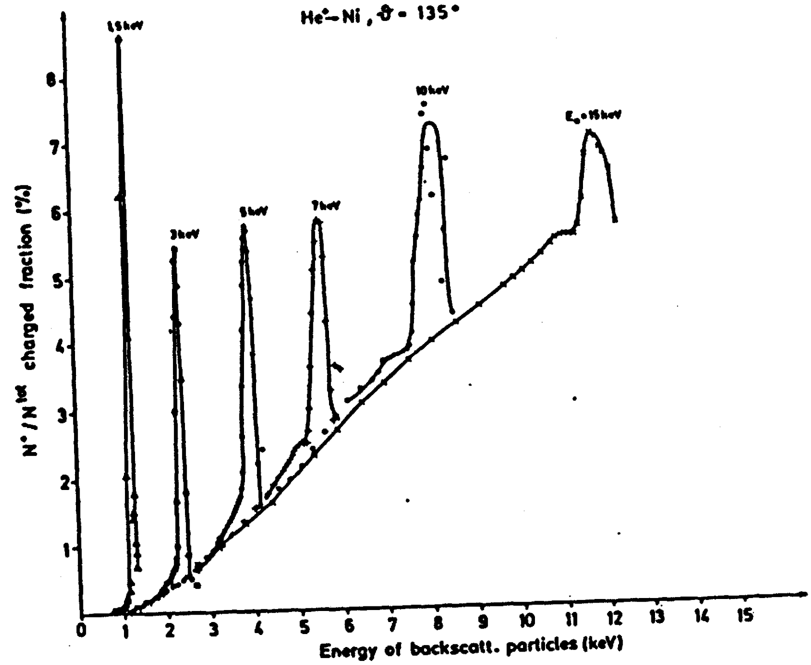

Fig. 3.4 Charge fraction of He backscattered from Ni at 135° for various incident energies (Ref.25).

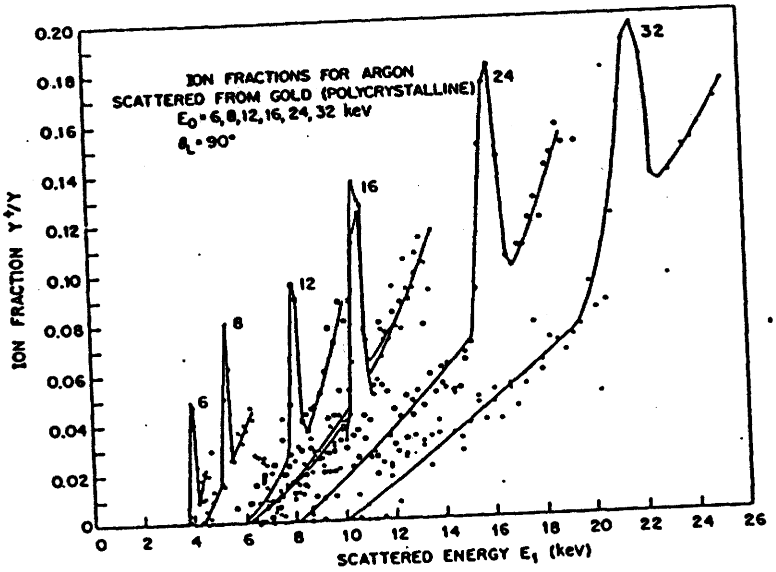

Fig. 3.5 Charge fraction of Ar backscattered from Polycrystalline gold at 90° for various incident energies (Ref.23).

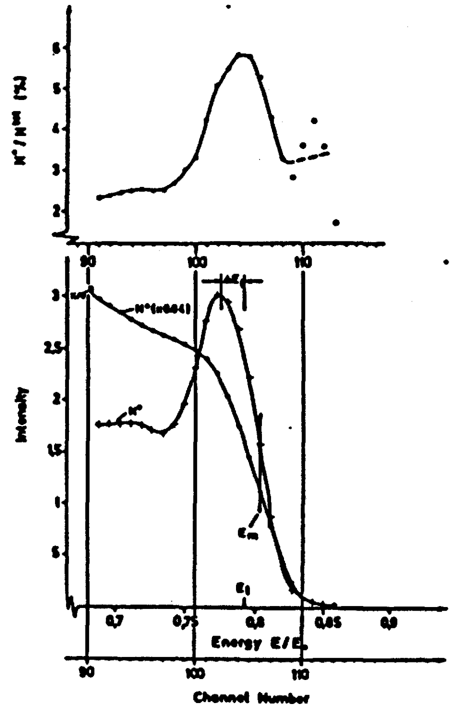

Fig. 3.6 Neutral and positive spectra of 7 kev He scattered by 135^o from Ni (Ref.25).

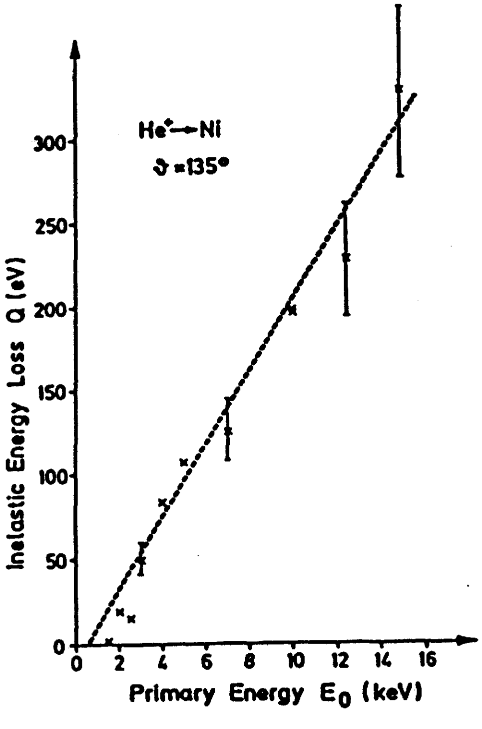

Fig. 3.7 Ineleastic energy loss of He backscattered by 135^o from Ni as a function of primary energy Eo (Ref.25).

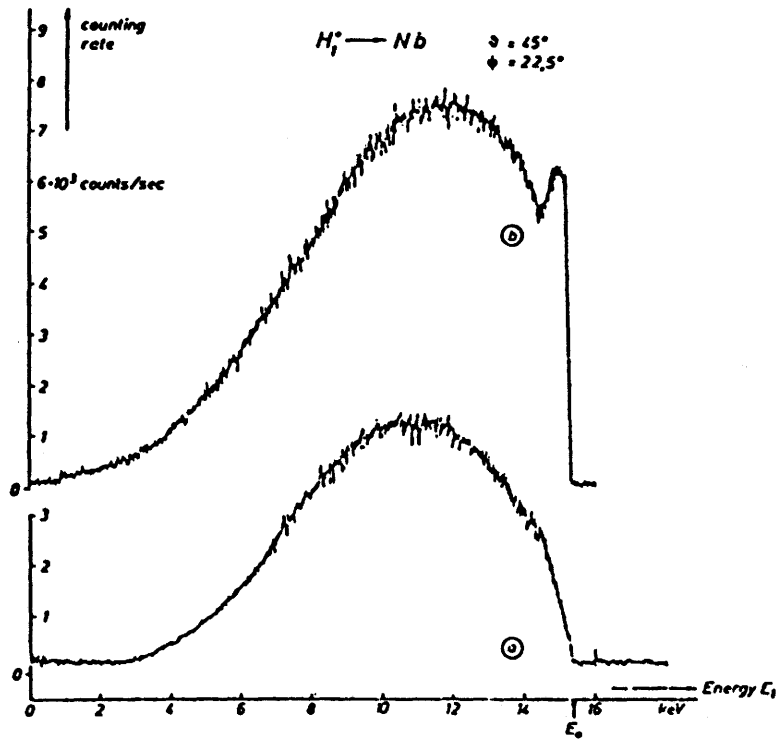

Fig. 3.8 Backscattering energy spectra of 15.36 kev H scattered from Nb: a. before heating
b. after heating
(Ref.27).

it's explanation support certain theoretical claims that the final charge state of the backscattered particles is reached at the surface.

The effect of molecular bombardment and target work functions on single and double electron capture probabilites was studied for H^+,H_2^+,H_3^+,D_1^+,D_2^+,D_3^+ incident on Au,Ta and ThO_2 (28). It was found that the probability for double electron capture increases with decreasing work function and that the ratio N^-/N^+ is larger than unity at low energies for Au and ThO_2. This ratio increased further when instead of atomic, molecular beams of equal energy per atom were used.

3.1.3 Radiation Damage Studies
(Reflection and Sputtering Coefficients)

The energy and material dependence of the reflection and sputtering coefficients are considered to be of critical importance in the planning of large plasma experiments. Together with other radiation damage parameters such as the energy reflection coefficient, they have been the focus of some experimental, but especially many semiempirical computer simulation studies.

Figure 3.9 shows the dependence of the energy reflection coefficient on the reduced energy . This figure contains a compilation of experimental data obtained with three entirely independent methods together with data from two machine calculations. All results agree to a stated 10% accuracy.

Figure 3.10 shows the angular dependence of the reflection coefficient. Verbeek (37) is responsible for the experimental data. He derived them by collecting energy spectra for a range of backscattering angles, and subsequently,

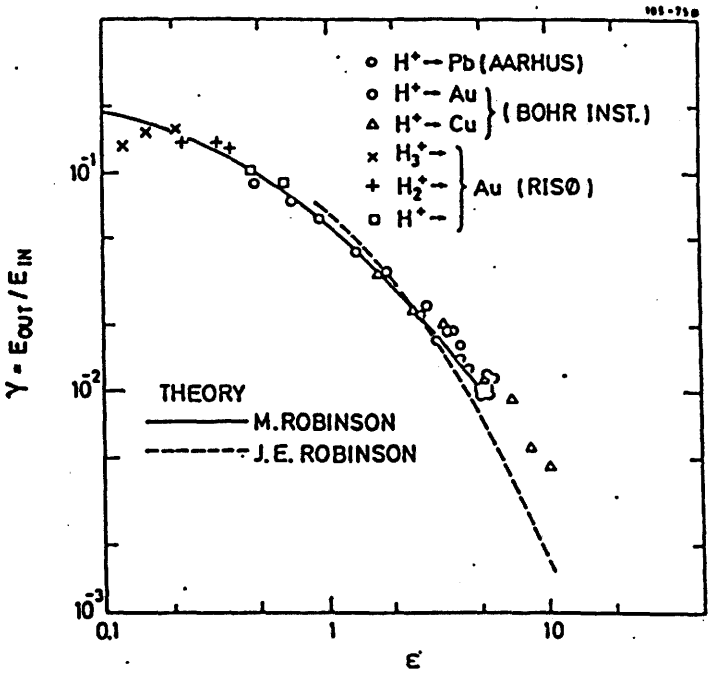

Fig. 3.9 The energy reflection coefficients as a function of the Thomas-Fermi reduced energy for protons scattered from a. Pb b. Au c. Cu. The theoretical calculations are for Cu by M. Robinson and Nb by J.E. Robinson. (Ref.34).

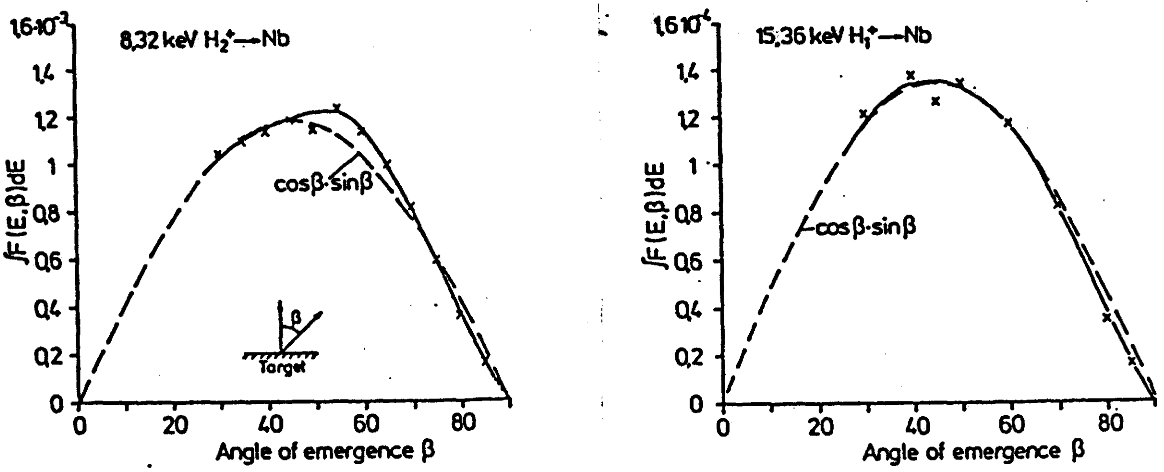

Fig. 3.10 Angular distribution of H scattered from Nb. The theoretical curves are due to J.E. Robinson (Ref.37).

integrating the energy distributions of the total number of backscattered particles over all energies. The theoretical results are due to a Monte Carlo calculation by Robinson (38,39).

Sputtering plays a very important role as a source of impuriites in a magnetically confined thermonuclear device. In a recent study, (45) the mean energy and shape of the secondary ion energy spectrum were investigated as a function of the primary energy and angle of emission. The results of this study indicate a sputtering behaviour which is different than that predicted by the random collision cascade theory. It was found that the peak in the distribution shifts with increasing primary energy and angle of emission.

CHAPTER 4

DESIGN OF THE LOW ENERGY ION SPECTROMER

4.1 The experimental apparatus

In experimental studies of ion reflection and sputtering, a particle beam of energy Eo is allowed to impinge on a target at an angle φ . The energy spectrum of the reflected and secondary ions may be measured as a function of the primary energy, the angle of reflection, the chemical composition of the target and the nature of the incident beam. The apparatus for such a study must contain (a) an ion source (b) a particle accelerator, (c) and interaction chamber kept at ultra high vacuum conditions (d) a system for the detection of individual events capable of classifying them according to their energy and (e) a means for varying the angles of incidence and emergence. The following sections describe the various components of the proposed LEIS apparatus.

4.2 The Particle Accelerator

An existing Kev particle accelerator was utilized for the generation of light ion beams. References 46 and 47 outline the design considerations and contain some of the construction specifications for this assembly. My intention here is to describe the functionality and operation of the component parts.

As Figure 4.1 indicates, the accelerator consisted of an R-F ion source (ORTEC Model 501), the beam optics, a mass analysis magnet (NEWPORT 1½" electromagnet) and a glass envelop. The ion source was capable of delivering a maximum current of 1ma. It operated by ionizing pure gas fed into the glass bottle through an inlet located at the base of the

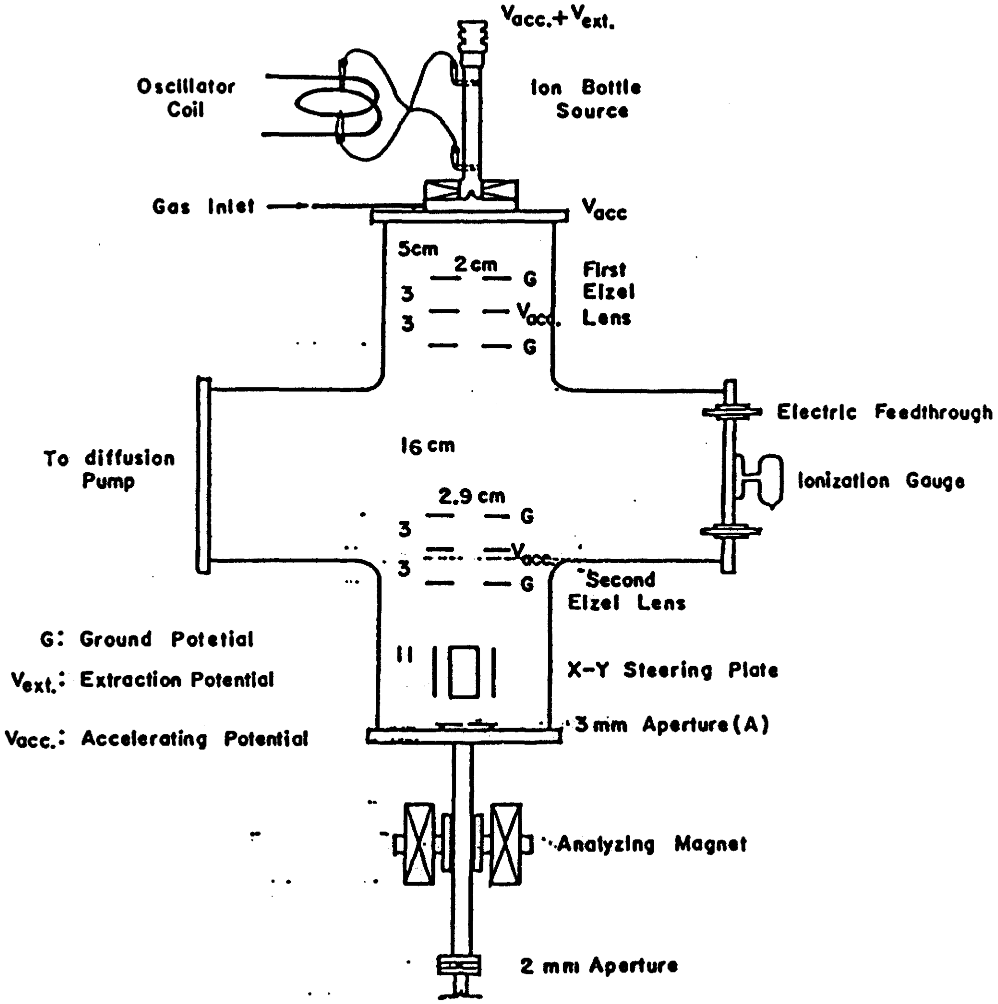

Fig. 4.1 Schematic diagram of particle accelerator (from Ref.46).

source. An R-F coil around the gas bottle generated the oscillating field which caused the gas to ionize by electron stripping. The positive ions were separated from the electrons by a 3kev extraction voltage applied between the head and the base of the source.

The purpose of the beam optics was to maximize the ion current at the target. It consisted of two Einzel lenses and two sets of deflection plates. The Einzel lenses focused the divergent beam exiting from the ion source and the deflection plates provided a means of aligning electrostatically the beam axis.

These parts were assembled inside a glass cross envelope which was pumped down to approximately 10^{-5} torr by an oil diffusion pump.

The focused beam was deflected and mass analysed by the Newport electromagnet. The calibration data for this magnet are included in Appendix A. Finally, a 2mm aperture at the exit of the accelerator defined the size of and collimated the beam.

4.3 The VACUUM SYSTEM

Two basic objectives were set in the design of the vacuum system: (a) the ultimate pressure in the interaction chamber was to be in the order of 10^{-11} torr and (b) the system was to have a fast target recycling time. It became obvious from reviewing the experimental work that ultra-high vacuum conditions are essential in surface studies since so many parameters are sensitive to the residual gas in the interaction chamber. The expedient examination of many different kinds of materials in a short time is the reason for the second requirement.

To achieve these objectives, the following were considered:

(a) system configuration
(b) pumping capacity
(c) material selection
(d) fabrication details

The large difference in pressure between the interaction chamber (10^{-11} torr) and the particle accelerator (10^{-5}torr) necessitates the three stage vacuum system configuration illustrated in Figure 4.2. The isolation chamber in the intermediate stage utilizes the differential pumping to impede the flow of gases from the first to the third stage. A 501/sec ion pump together with an auxiliary Ti sublimation or a cryopump could maintain a pressure of 10^{-8} torr in the second stage. The purpose of the auxiliary pump is the removal of active gases and especially hydrocarbons from the vacuum system in order to minimize carbon deposition on the target. Agamy (46) employed a 2000 l/sec Ti sublimation with this configuration and he was able to achieve a pressure of 10^{-8} torr in the isolation chamber.

All of the materials utilized in the second and third stages were selected so that they could withstand baking at 200-300^{0}C for extended lengths of time. Baking drives off gas adsorbed on the surfaces and absorbed within the solid materials. This reduces considerably the pump down time. Another consideration in the selection of the materials was that they would have a very low outgassing rate.

Since stainless steel 304 after vacuum bake out at 250^{o}C outgasses at a rate of $2\text{x}10^{-12}$ torr l/sec (48) a pressure in the 10^{-10} torr region can be achieved in the UHV chamber by providing a pumping capacity of 1 l/sec for each 100 cm^2 of surface area. The constructed interaction chamber has a total inside surface area of approximately 4250 cm^2 and the area of all the instruments in it is estimated to be

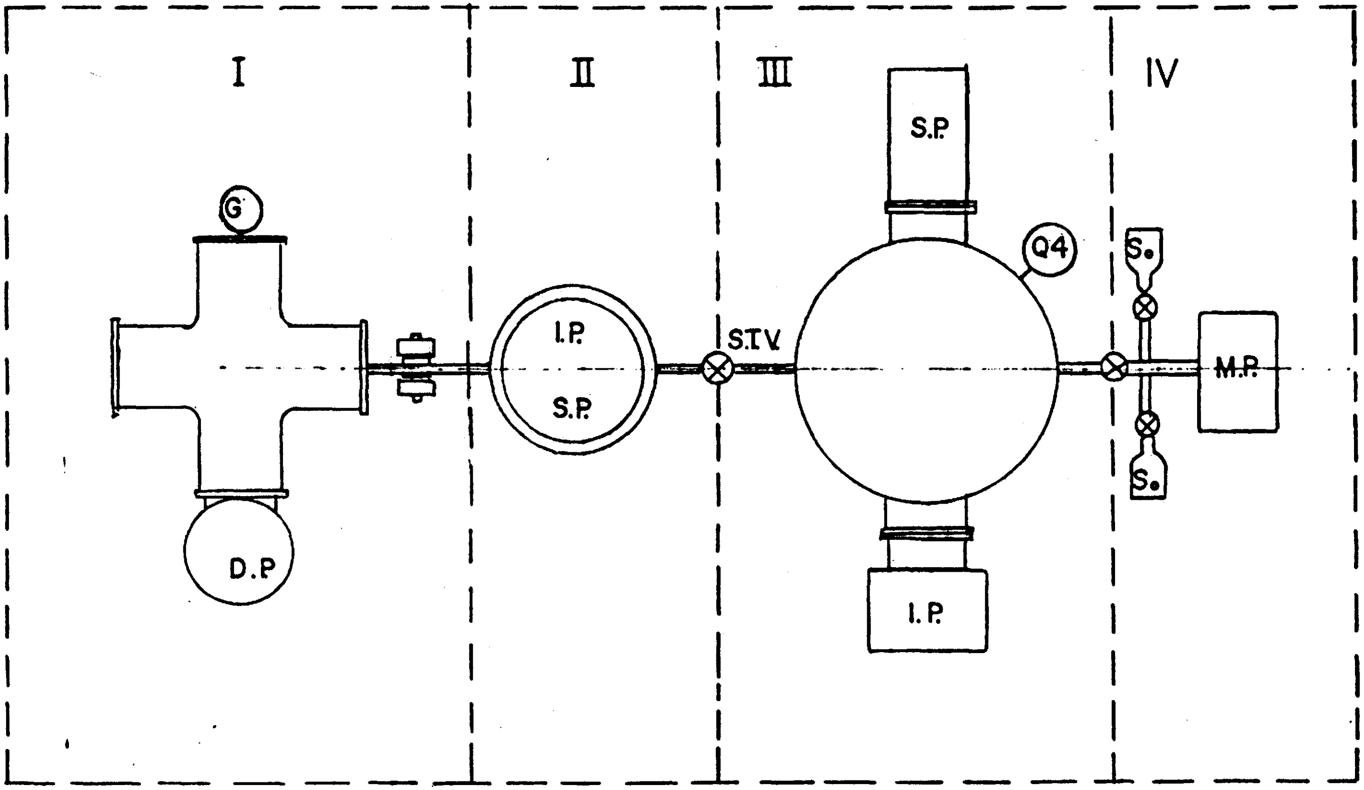

LEGEND

G	IONIZATION GAUGE
D.P	DIFFUSION PUMP
I.P.	ION PUMP
S.P	SUBLIMATION PUMP
S.	SORPTION PUMP
M.P.	MECHANICAL PUMP
Q4	QUADRUPOLE MASS SPECTROMETER

Fig. 4.2 The vacuum system.

another 5000 cm^2. Assuming all parts to be made of stainless steel 304, then selecting a 100 l/sec ion pump should be adequate to maintain the required steady state pressure level of 10^{-10} torr. In addition, operating a 2000 l/sec $\overset{\text{Ti}}{T_i}$ sublimation pump temporarily, should further reduce the pressure by more than one order of magnitude (48) down to the ultimate level of 10^{-11} torr.

In Reference (50) H.J. Halama describes a vacuum system having approximately half the surface area of our vacuum chamber. He was able to achieve a pressure of approximately 10^{-11} torr using a 20 l/sec ion pump together with a $\overset{\text{Ti}}{T_i}$-ball sublimation pump. He found that the main limitation in the ultimate pressure of the system was determined by the ability of the Ti film to pump H and methane gases.

Roughing of the system from atmospheric pressure was accomplished by the mechanical forepump (M) and the two sorption pumps (S_1,S_2). A liquid nitrogen cooled trap prevented oil vapours from contaminating the UHV chamber.

Since in a surface experiment it is more important to know the partial pressure of the residual gases than the total pressure, a quadrapole mass spectrometer (Q4) was used for gas analysis of the UHV chamber.

The straight-through valve (V) isolated the interaction chamber from the rest of the system when it was brought up to atmospheric pressure for a change of targets. Furthermore, by making the target holders compatible to the quick load device pioneered by J.E. Robinson (51) the targets could be recycled into the UHV chamber without disturbing the vacuum level.

4.4 The Goniometer

A high precision target manipulator was designed with the following features:

(1) Control of the target orientation about two perpendicular axes.

(2) Tilting from -90° to $+90^{\circ}$ about the incident beam.

(3) Rotation from -45° to $+45^{\circ}$ about the target normal.

(4) Angular accuracy and repeatability of settings to 0.1°.

(5) Accurate beam definition and directional control of the angle of incidence.

The goniometer (Figure 4.4) consists of two high precision feedthroughs and a gear coupling mechanism assembled on the top flange of the UHV chamber. The linear motion feedthrough (Varian 954-5049) provides the rotational control over the target. It is connected by a shaft extension to a rack and pinion assembly (Figure 4.8) translating linear to rotational motion. To prevent vacuum freeze the dove-tailed slide supporting the rack was constructed from Inconel whereas the material used for the mating case was SS304.

The case is bracketed on a bearing housing which has 360° rotational freedom. A set of anti-backlash gears coupled this housing to the rotary motion feedthrough (Varian 954-5151). A linear bearing was inserted at the target end of the housing to minimize the deflection of the shaft pushing on the slide. Machining tolerances were taken up by spring loading, where necessary.

The adjacent component shown in the assembly drawing 4.4 is a proposed mechanism which was to be used for defining the beam accurately just before impinging on the target and for controlling the direction of incidence.

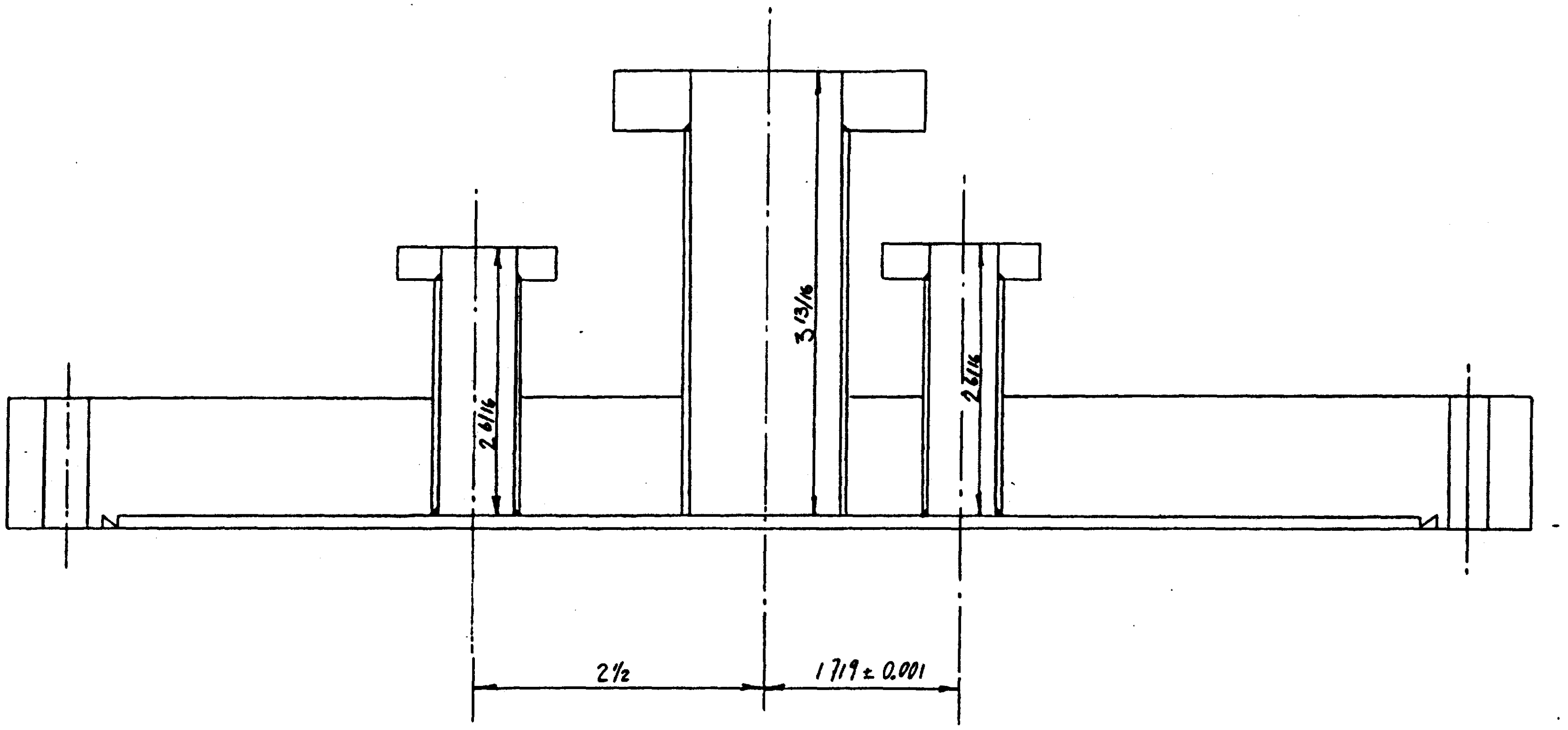

FIG. 4-3 TOP FLANGE A-A

Fig. 4.4 Assembly drawing of the goniometer.

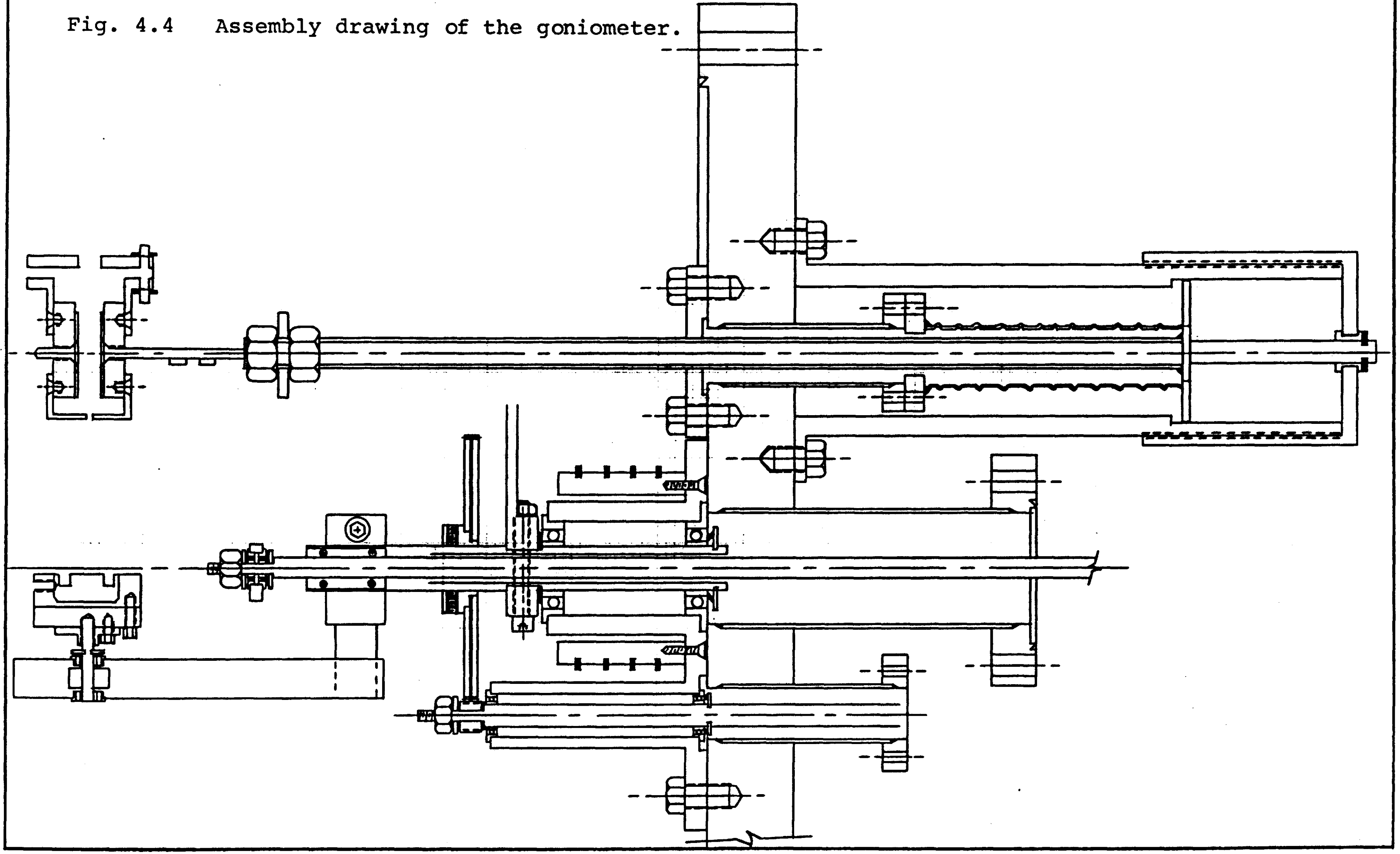

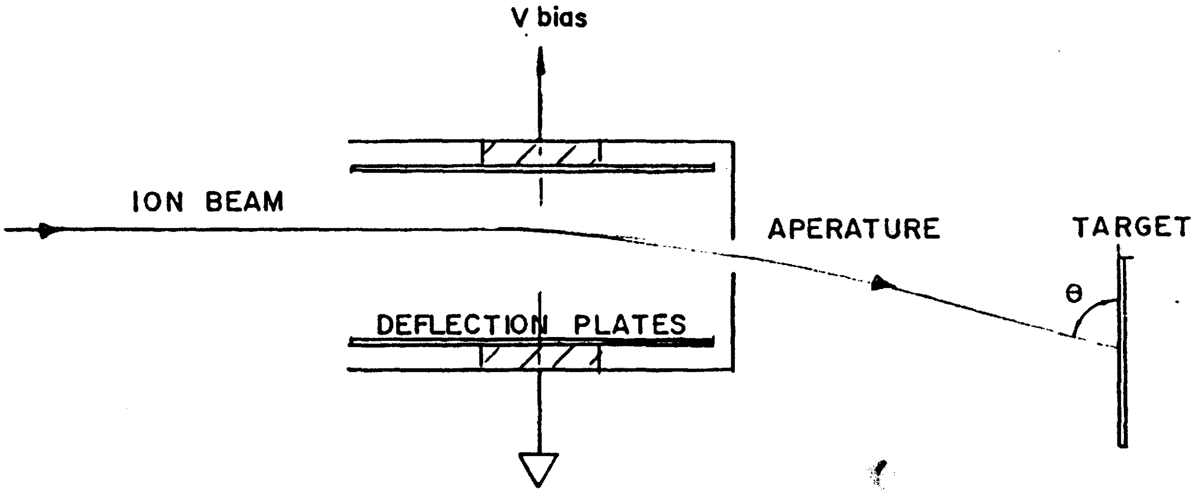

Fig. 4.5 The voltage V across the deflection plates determine the angle of incidence.

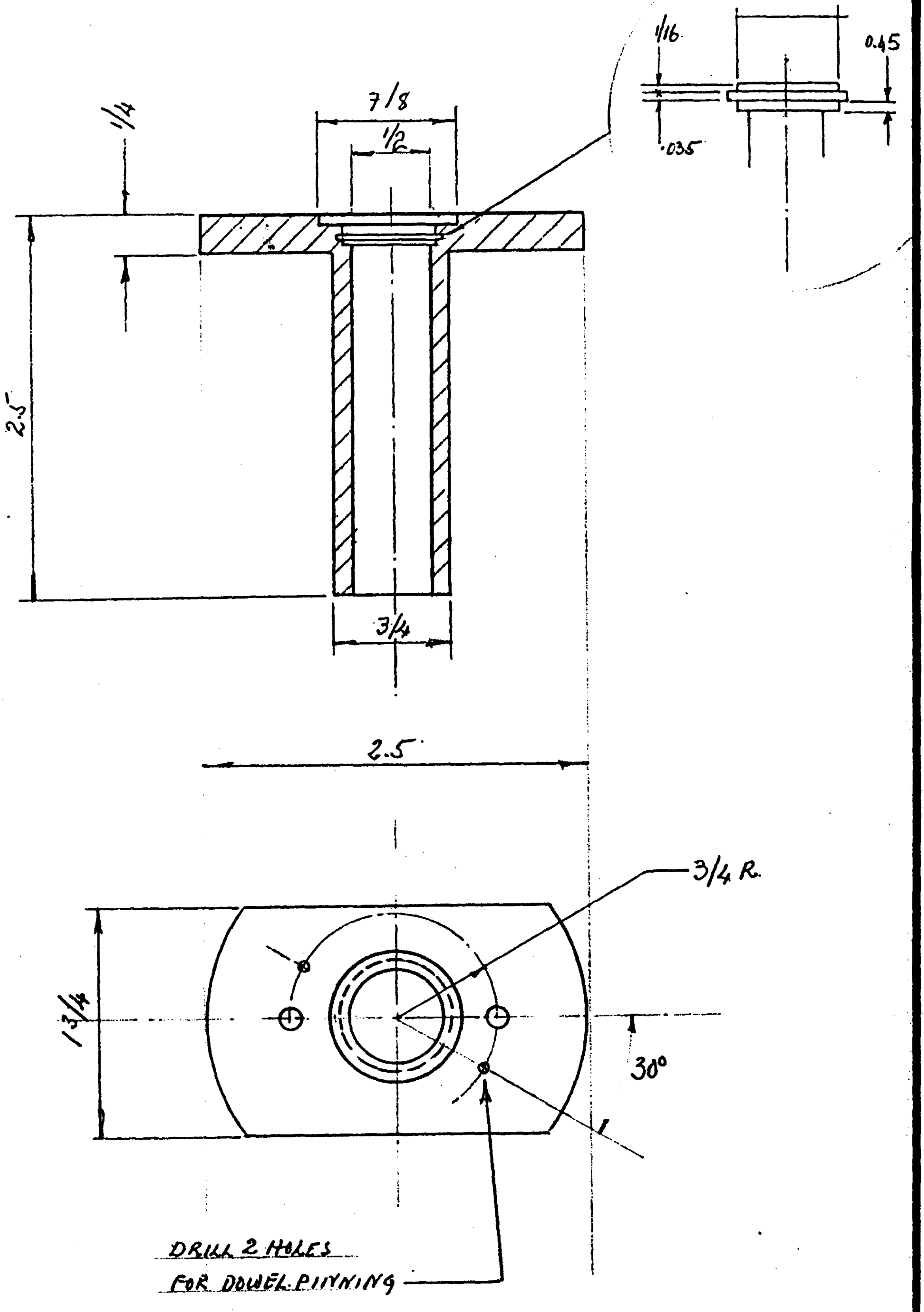

Fig. 4.6 Bearing housing for rotary feedthrough shaft.

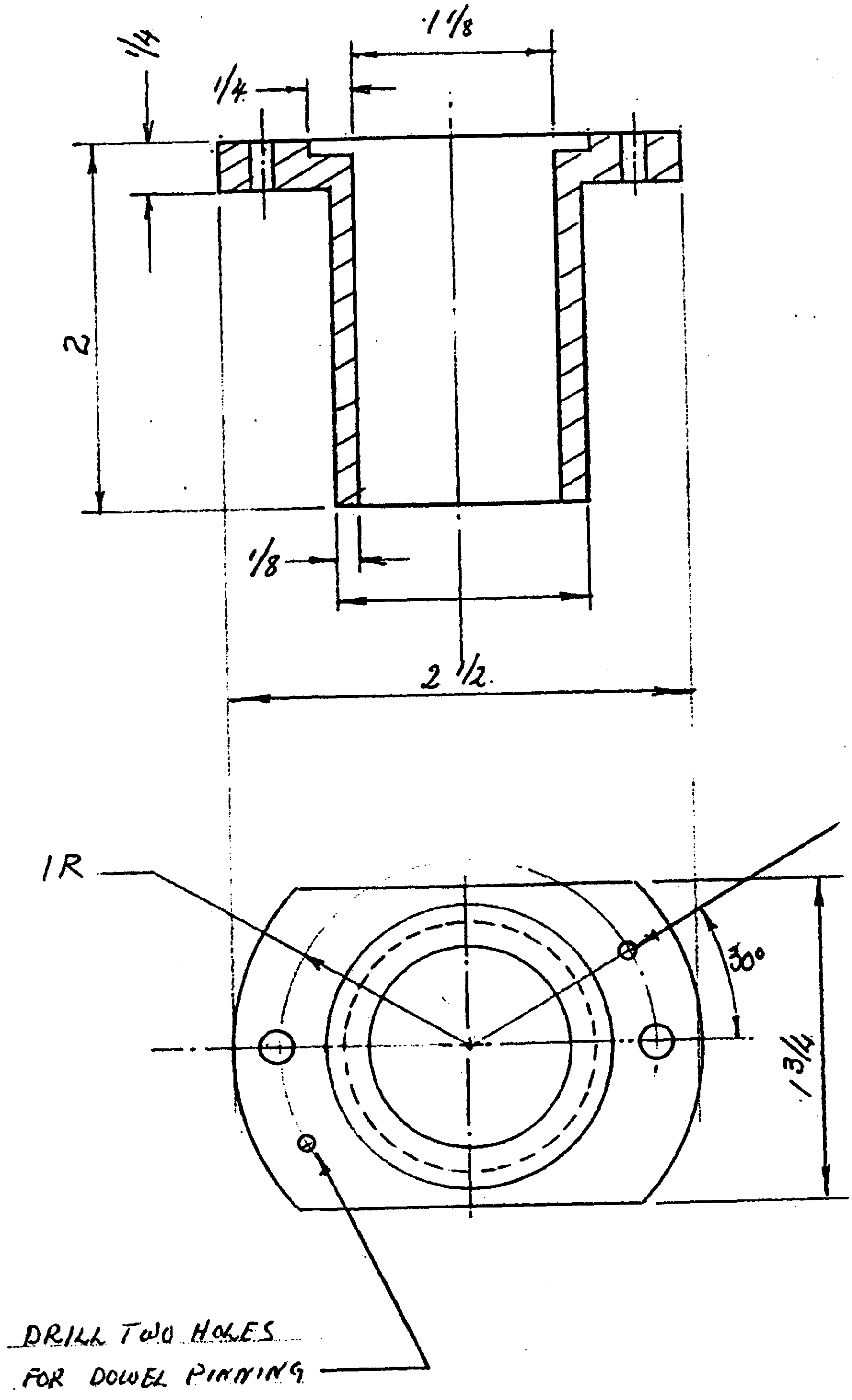

Fig. 4.7 Bearing housing for linear feedthrough shaft.

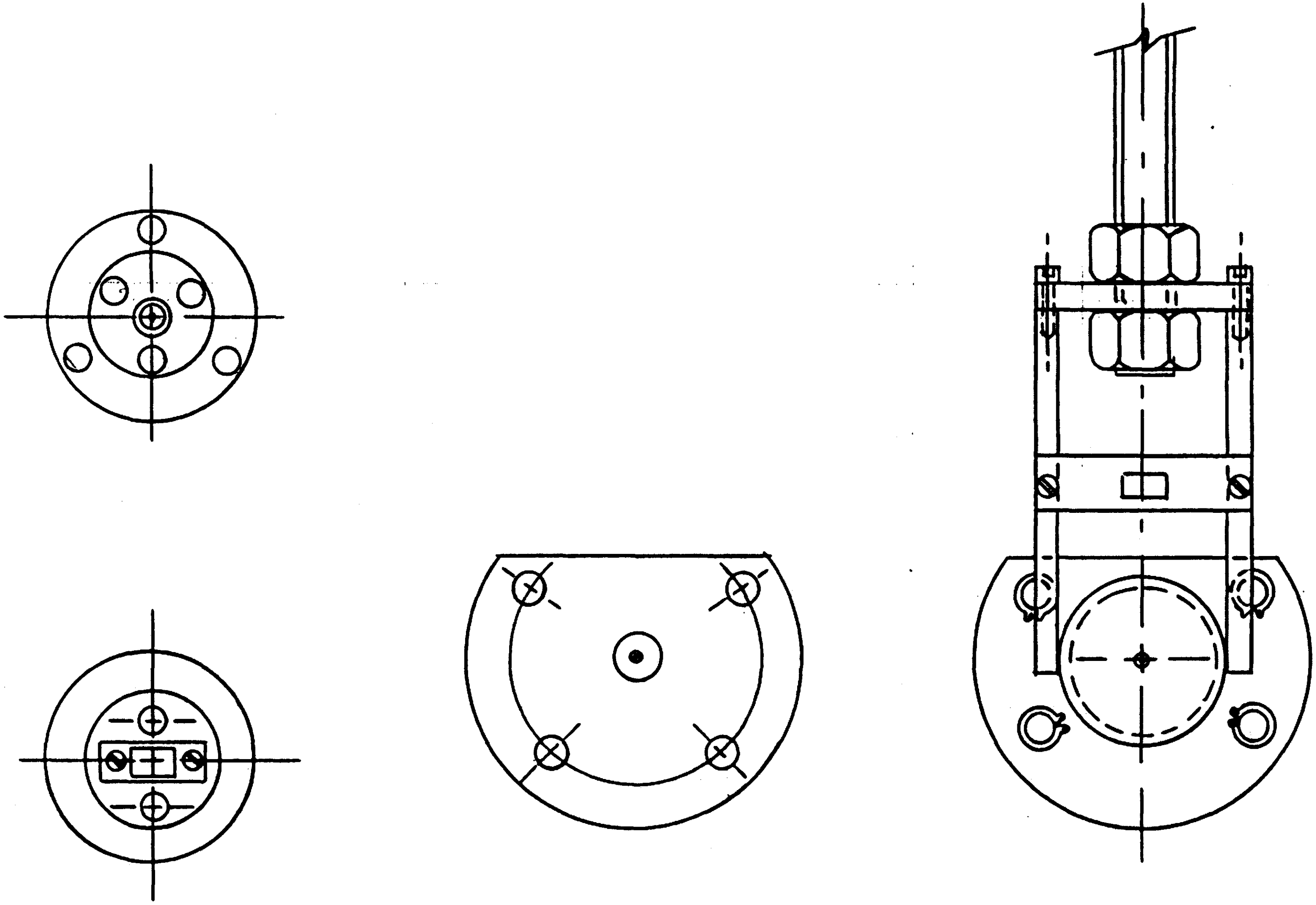

Fig. 4.9 Details for deflection plates housing.

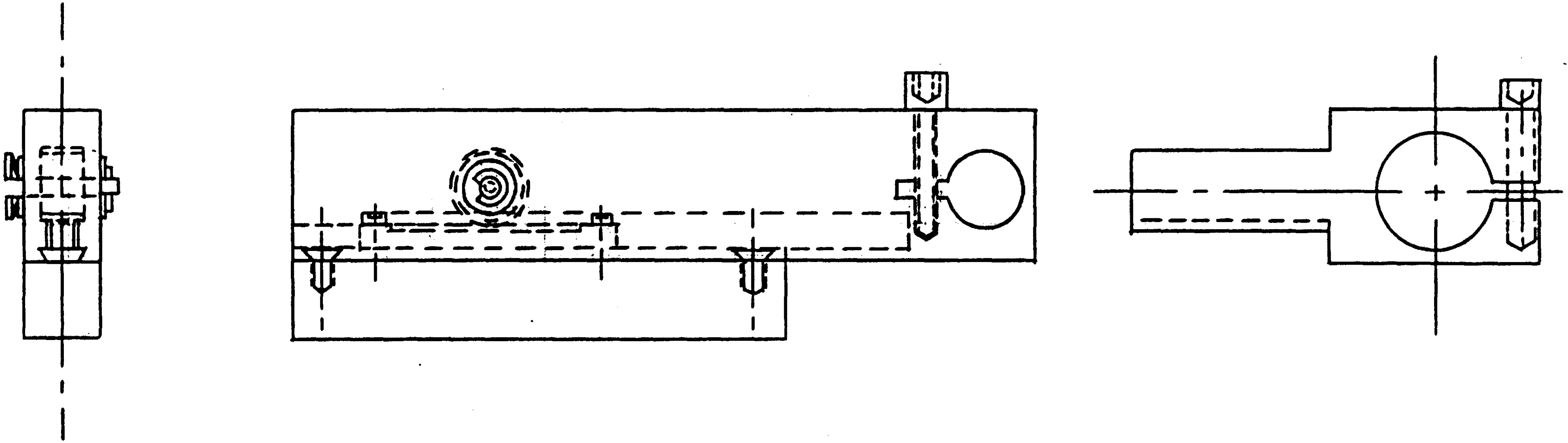

Fig. 4.8 Assembly drawing for rack and pinion mechanism.

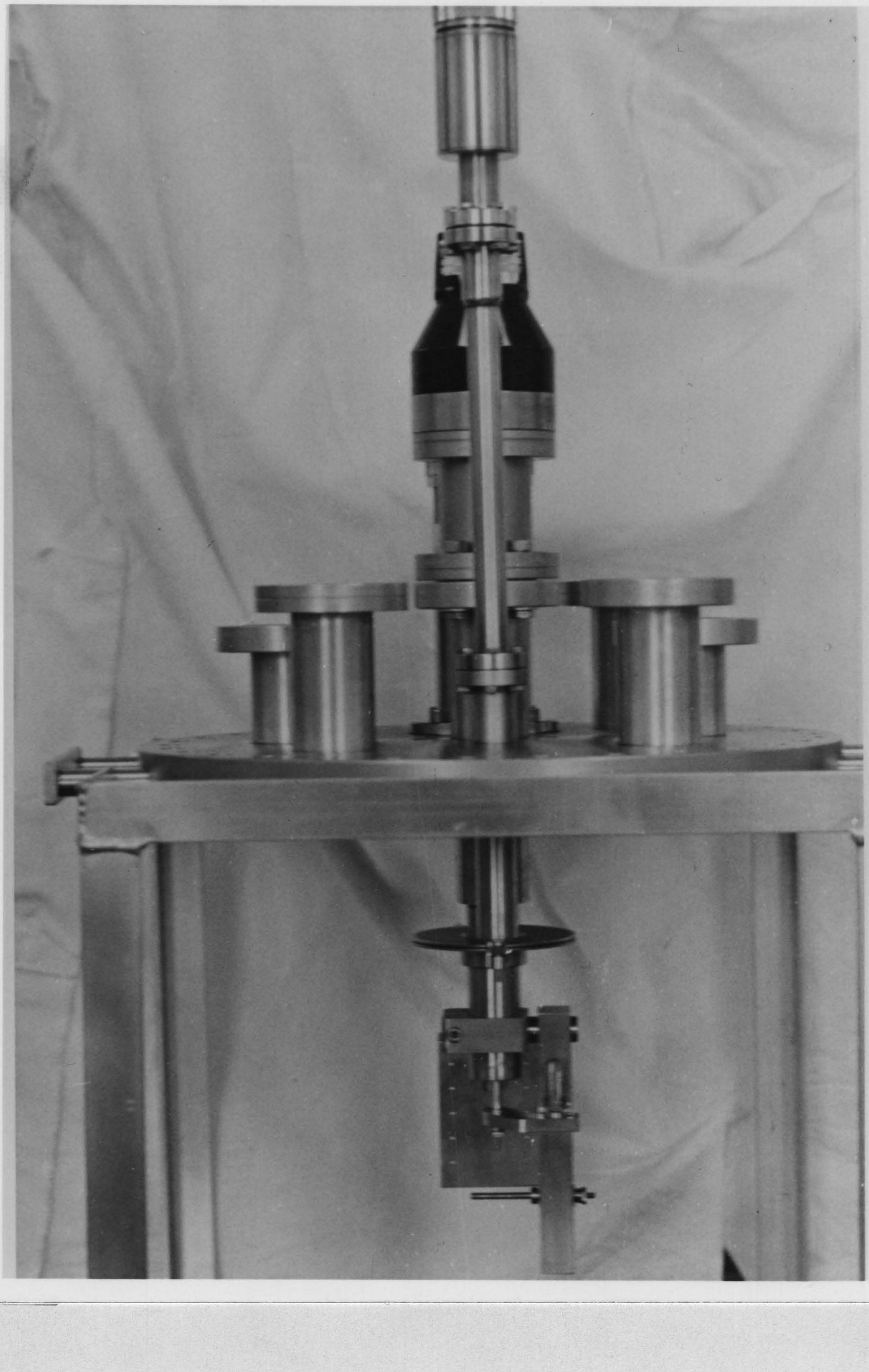

Figure 4.10 Photograph showing goniometer assembled on top flange.

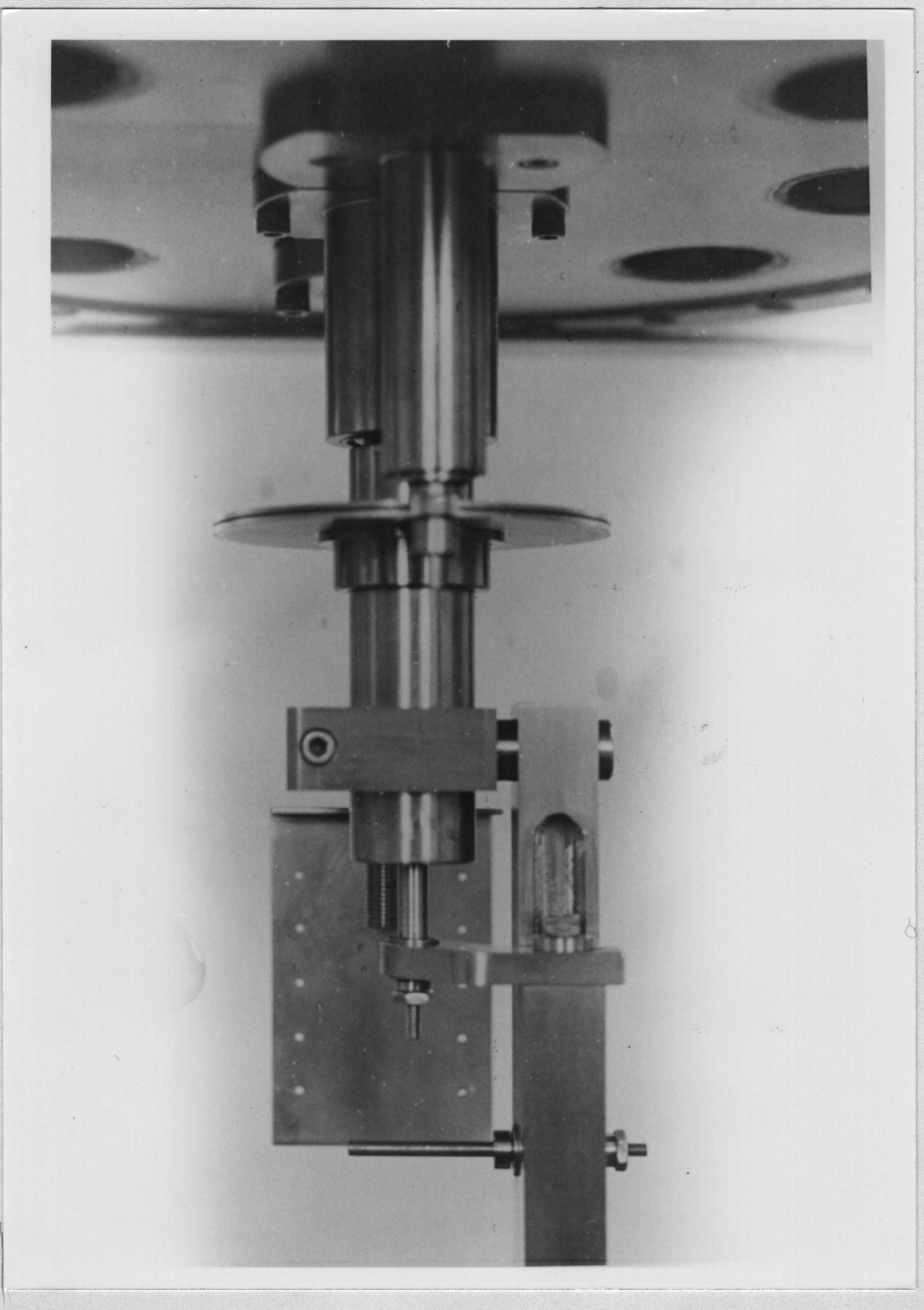

Figure 4.11 Close up photograph of goniometer.

It consists of a cage with a slit on one side, parallel deflection plates in the middle and an apperature on the other end. Flexible bellows allow vertical movement of the cage. As Figure 4.5 illustrates, adjusting the deflection voltage enables aligning of the beam with the apperture. This corresponds to tilting the target about the horizontal axis normal to the direction of the beam.

The sample holder was designed so that it was compatible with the fork mechanism of the quick load device. Also provision were made which would enable in situ heating of the taget by a tungsten filament. Figure 4.10 is a photograph of the goniometer as was constructed.

4.5 The Analyser Table

The cylindrical UHV chamber was covered by two 13¼" flanges. The top flange was used for suspending the goniometer and the bottom one for supporting the analyser table. This assembly provided the following features:

(1) mechanical support for the hemispherical electro-static analyser and the channeltron housing.

(2) full 360° rotational freedom of the ESA about the chamber vertical axis.

(3) a means of providing continuity between an electrical feedthrough on the bottom flange and the ESA and detector without interfering with requirement number 2.

Figure 4.14 is a photograph of the analyser table. The picture shows that the table consists of two platforms. The lower one is fixed on the bottom flange and contains a ring collar with three roller bearing contacts on which the upper platform rotates. A mechanism consisting of a large 144 tooth gear, a worm gear and two miter gears

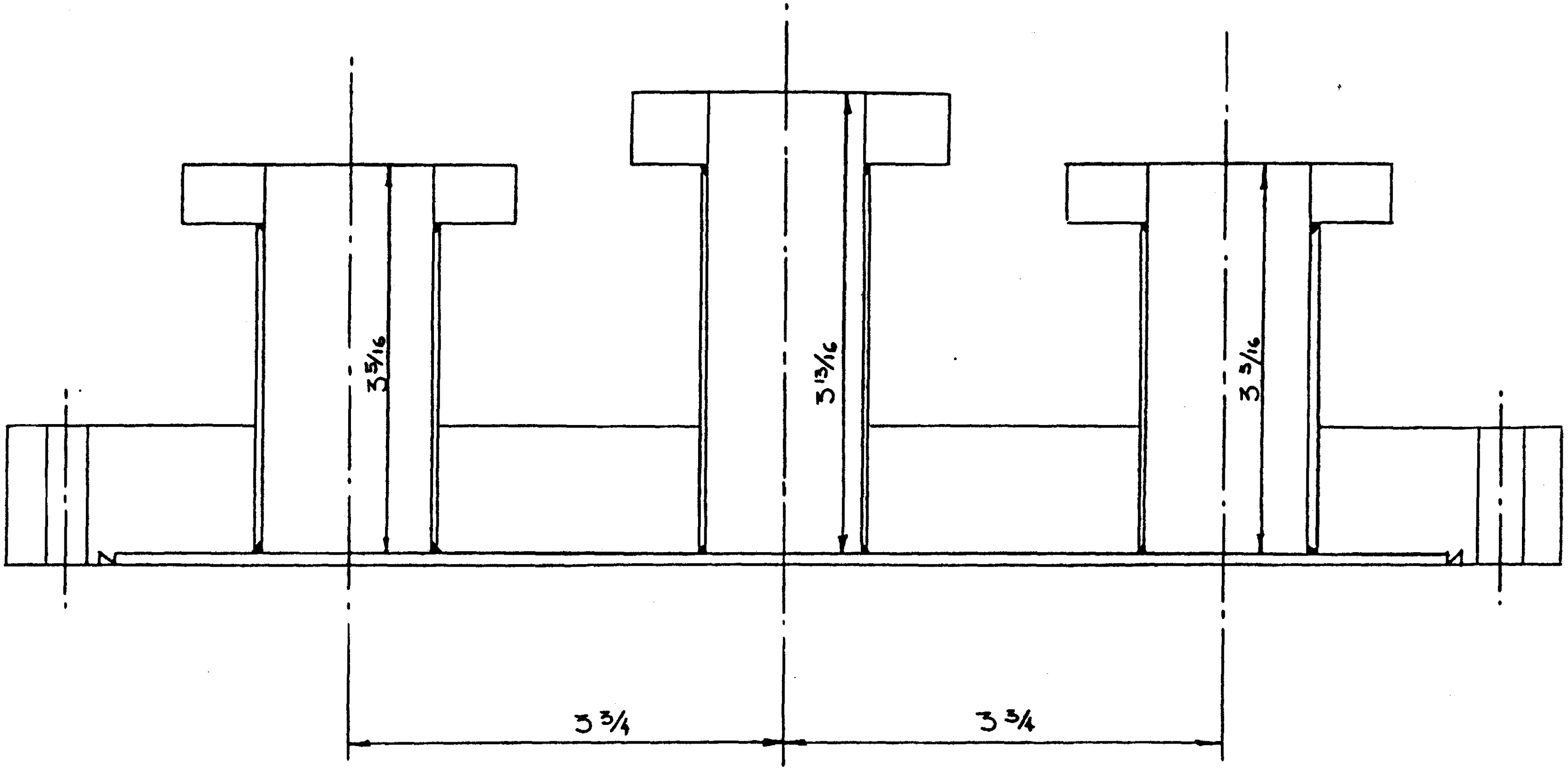

FIG. 4-12 BOTTOM FLANGE C-C

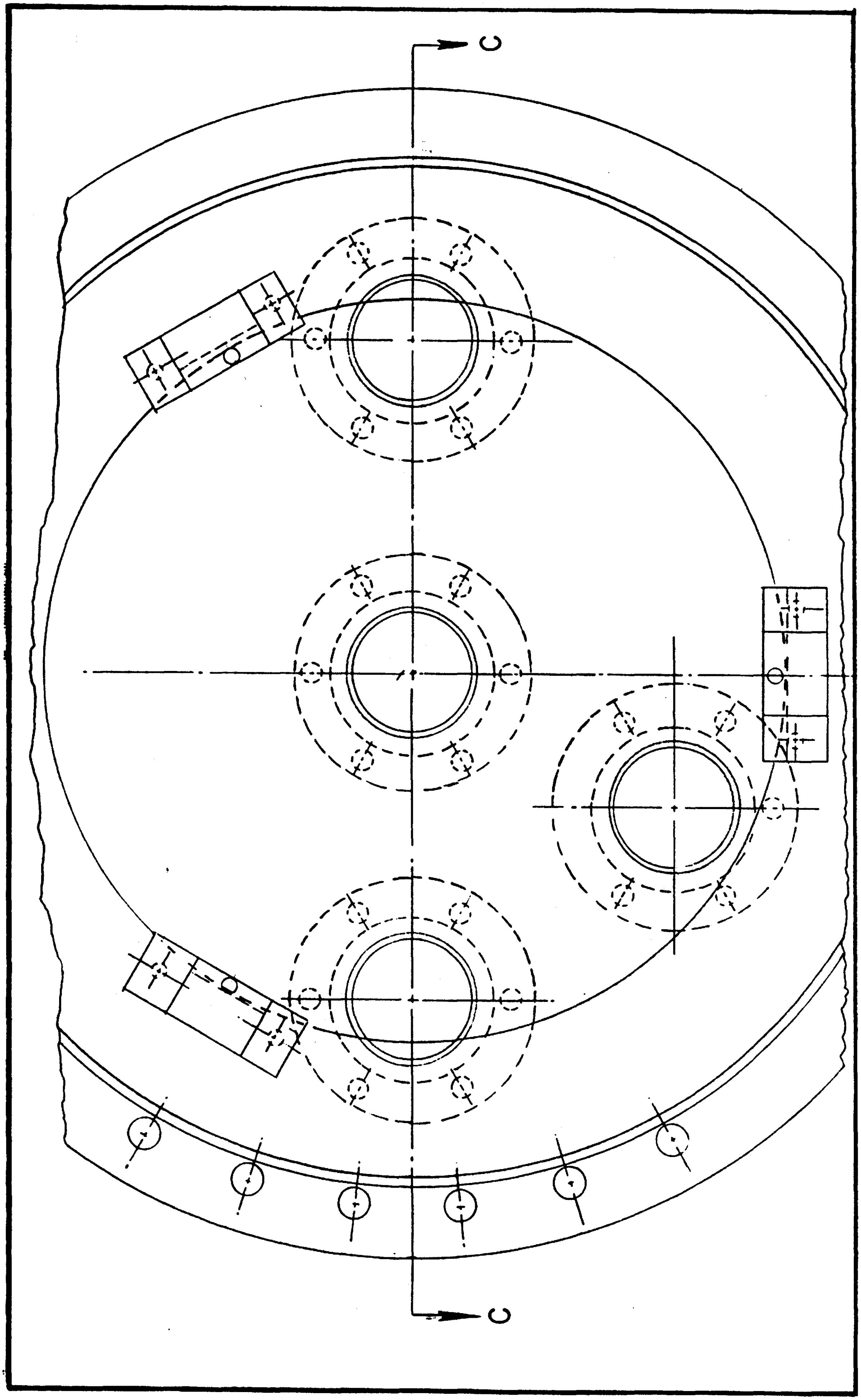

Fig. 4.13 Bottom flange

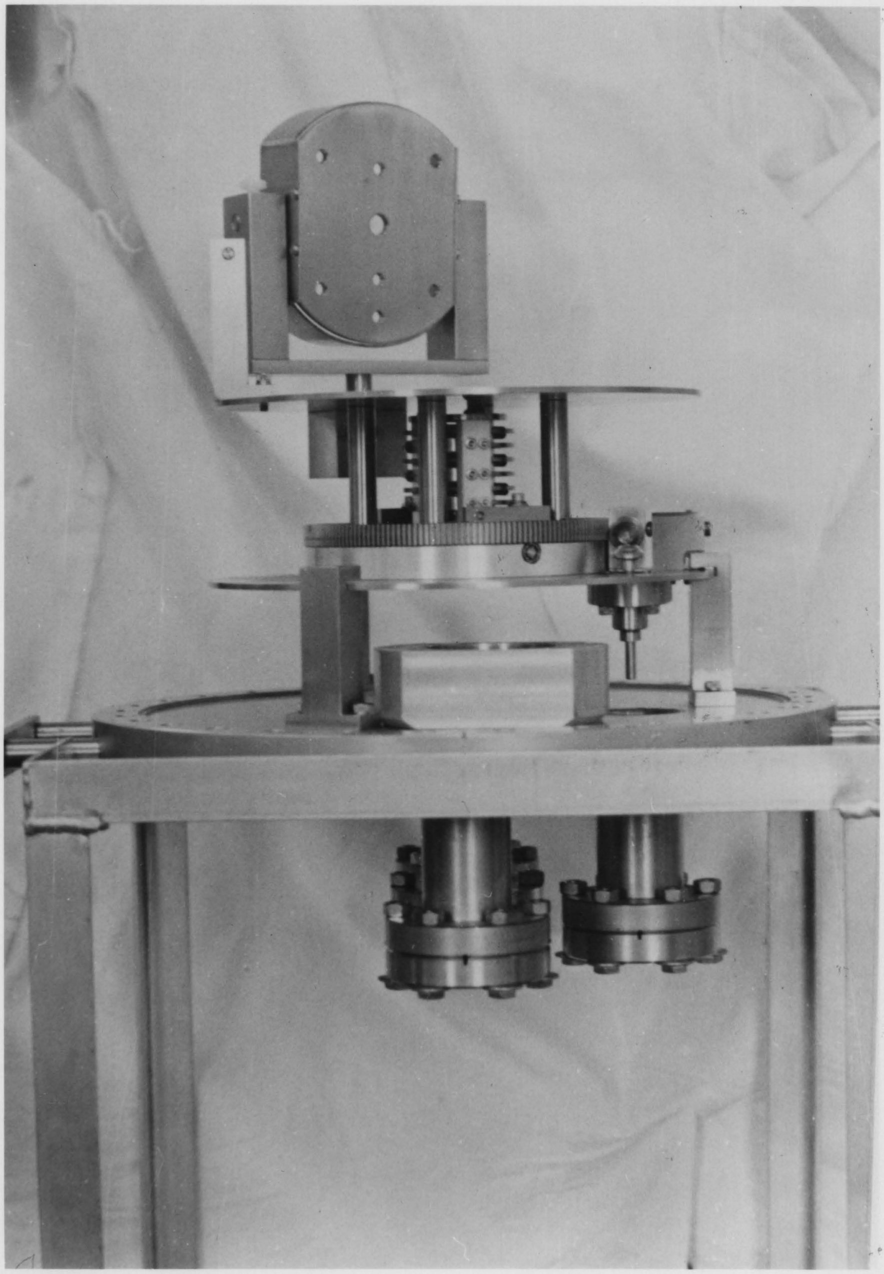

Figure 4.14 Photograph showing analyser table assembled on bottom flange.

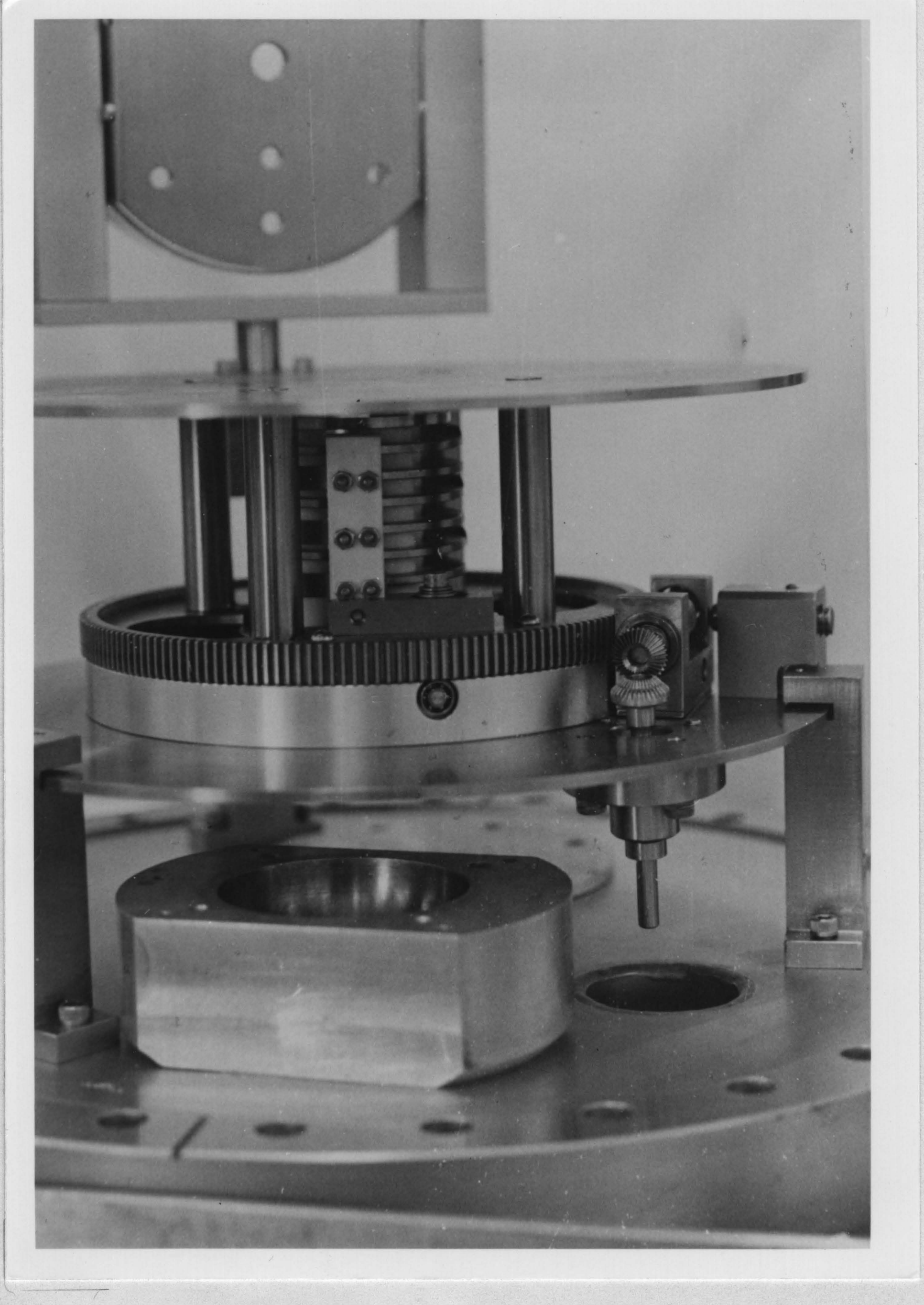

Figure 4.15 Close up photograph of analyser table.

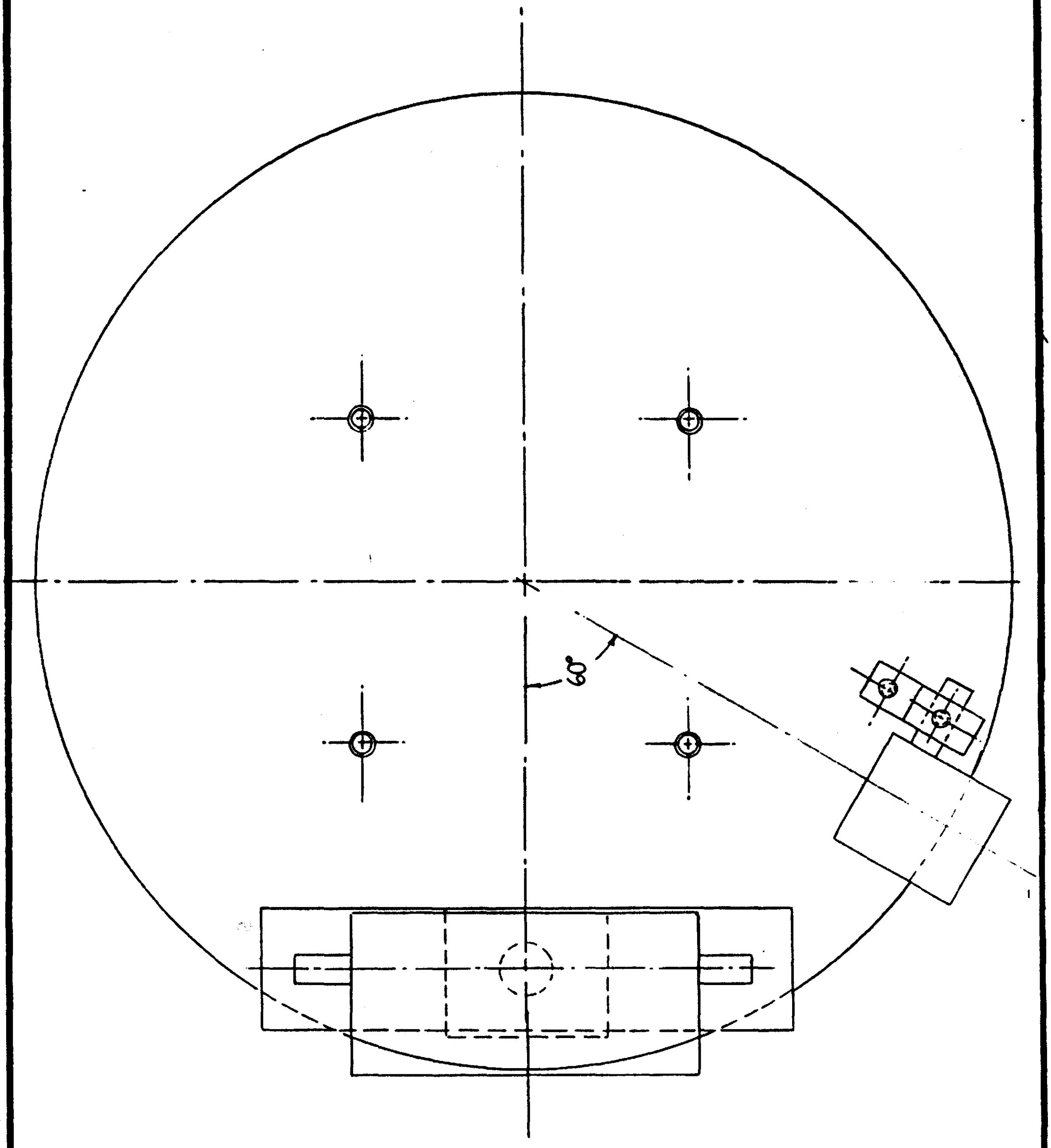

Fig. 4.16 Assembly drawings of upper platform of analyser table.

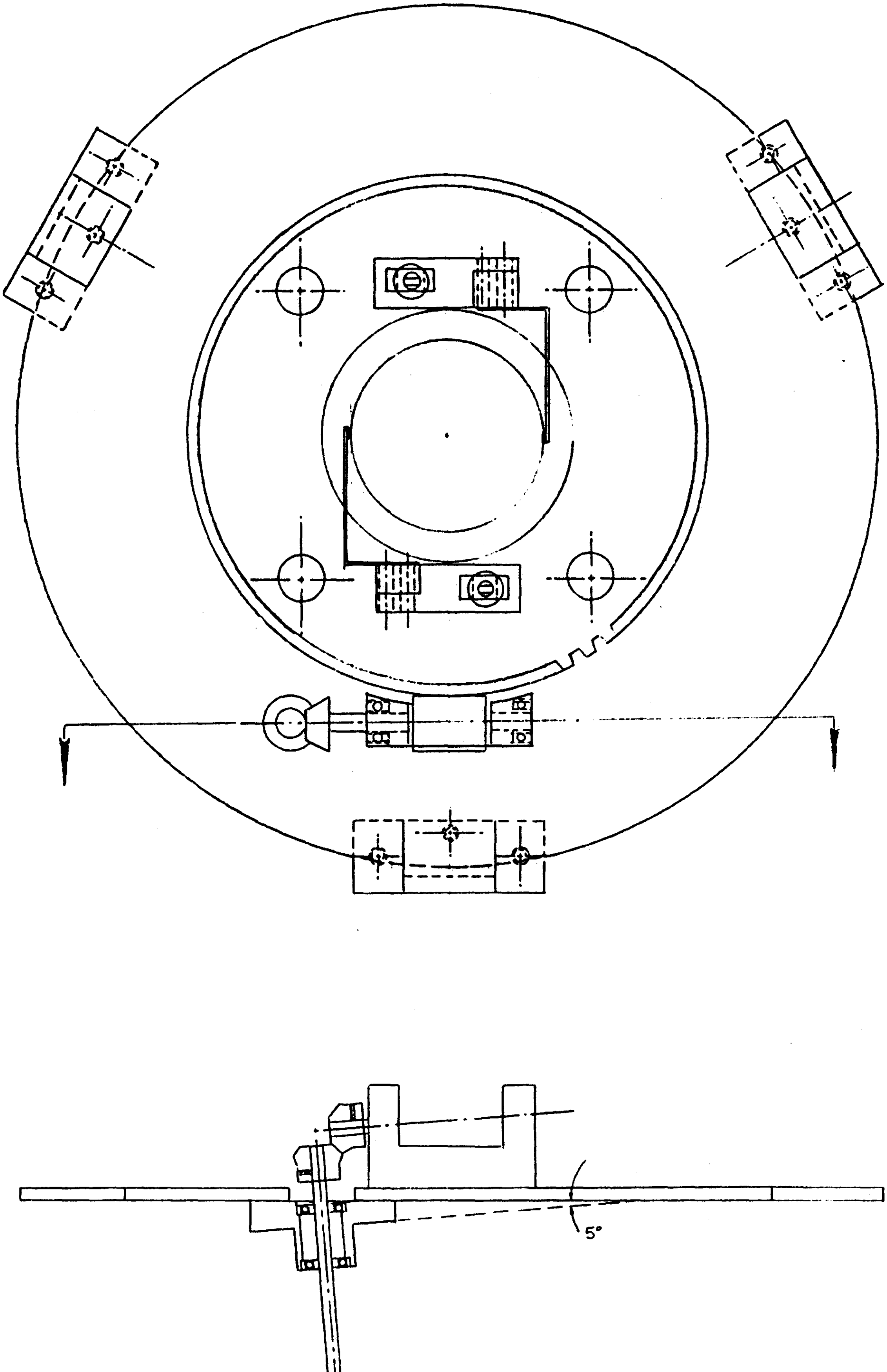

Fig. 4.17 Assembly drawing of lower platform of analyser table.

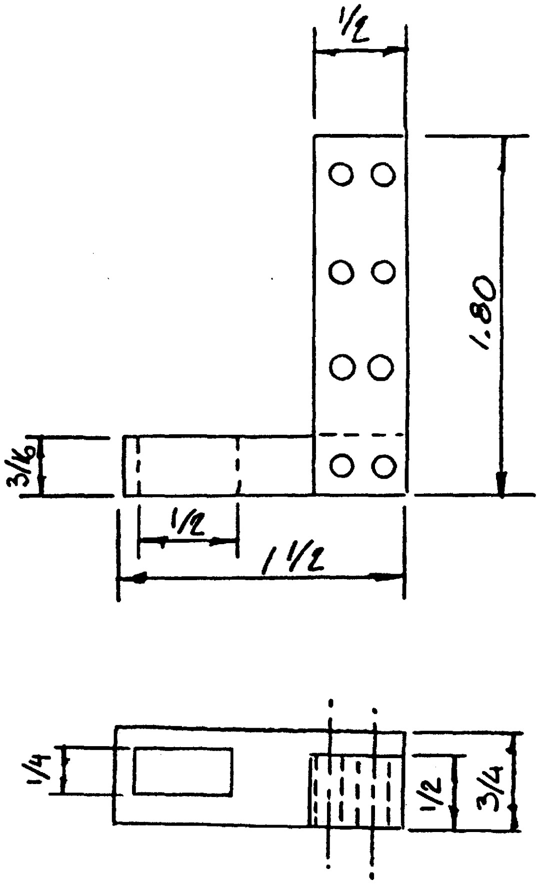

Fig. 4.18 Assembly drawing of contact bracket for rotary switch.

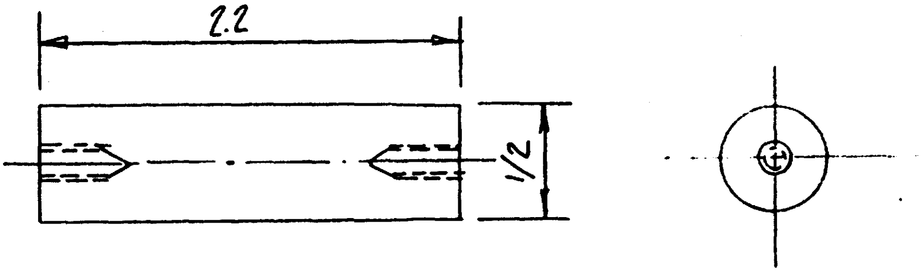

Fig. 4.19 Metal stand off.

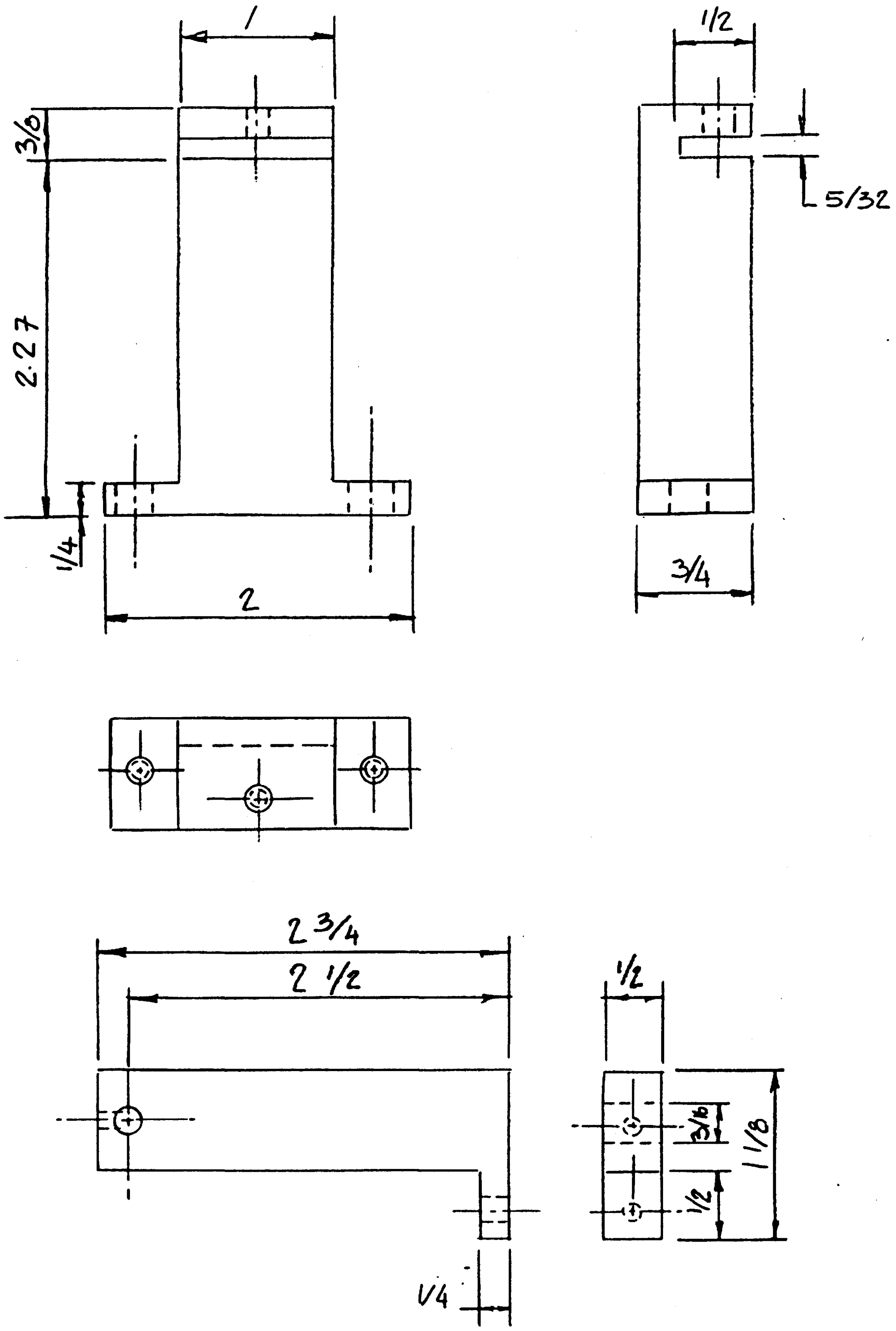

Fig. 4.20 Analyser table legs

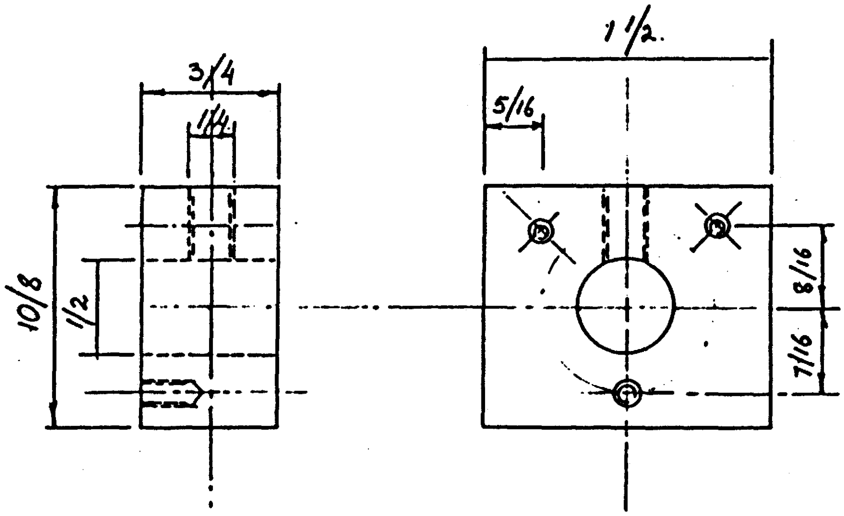

Fig. 4.21 Support for analyser fork.

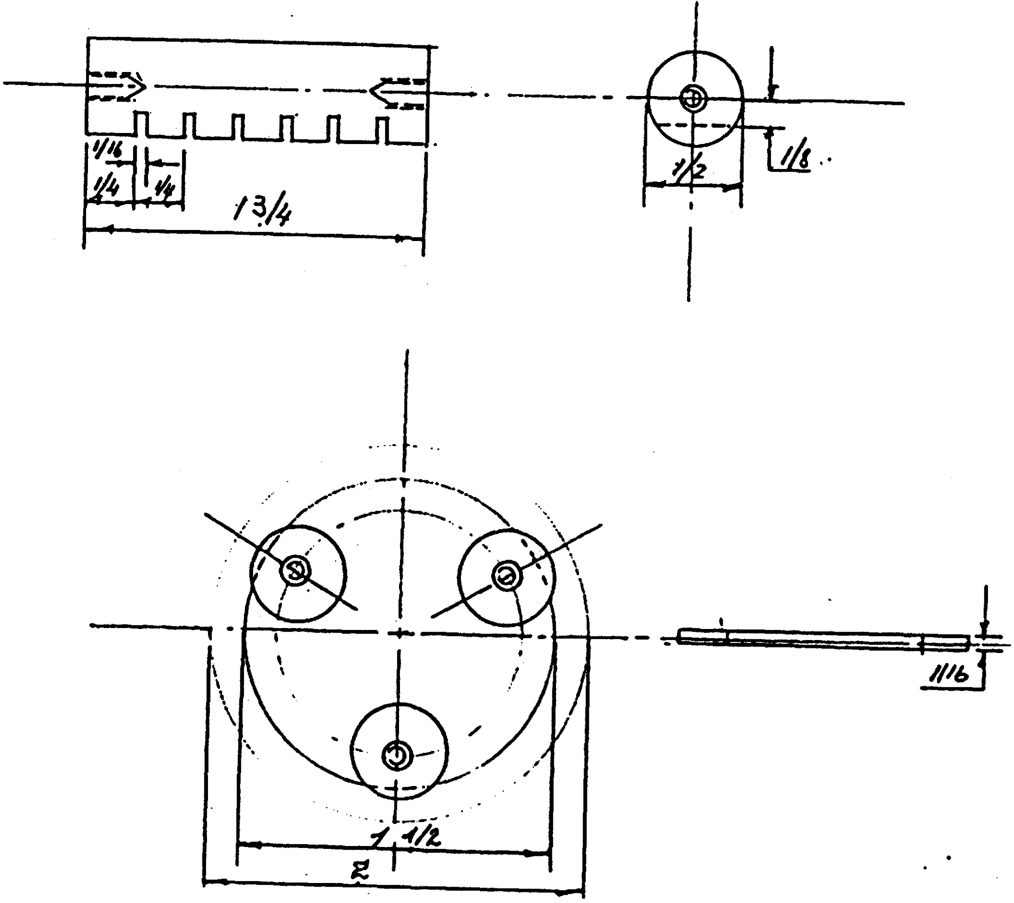

Fig. 4.22 a. Assembly drawing of rotary contact switch.
b. Ceramic standoff
c. Nickel ring

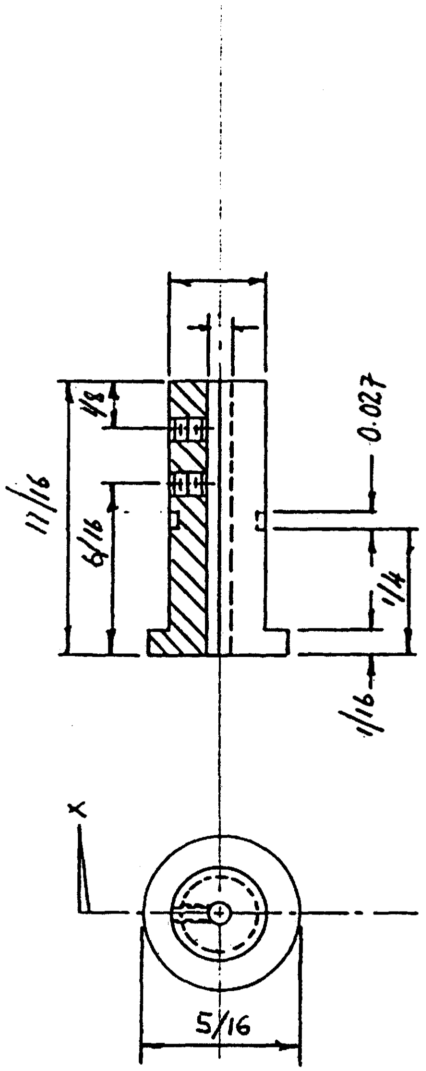

Fig. 4.23 Electrical feedthrough.

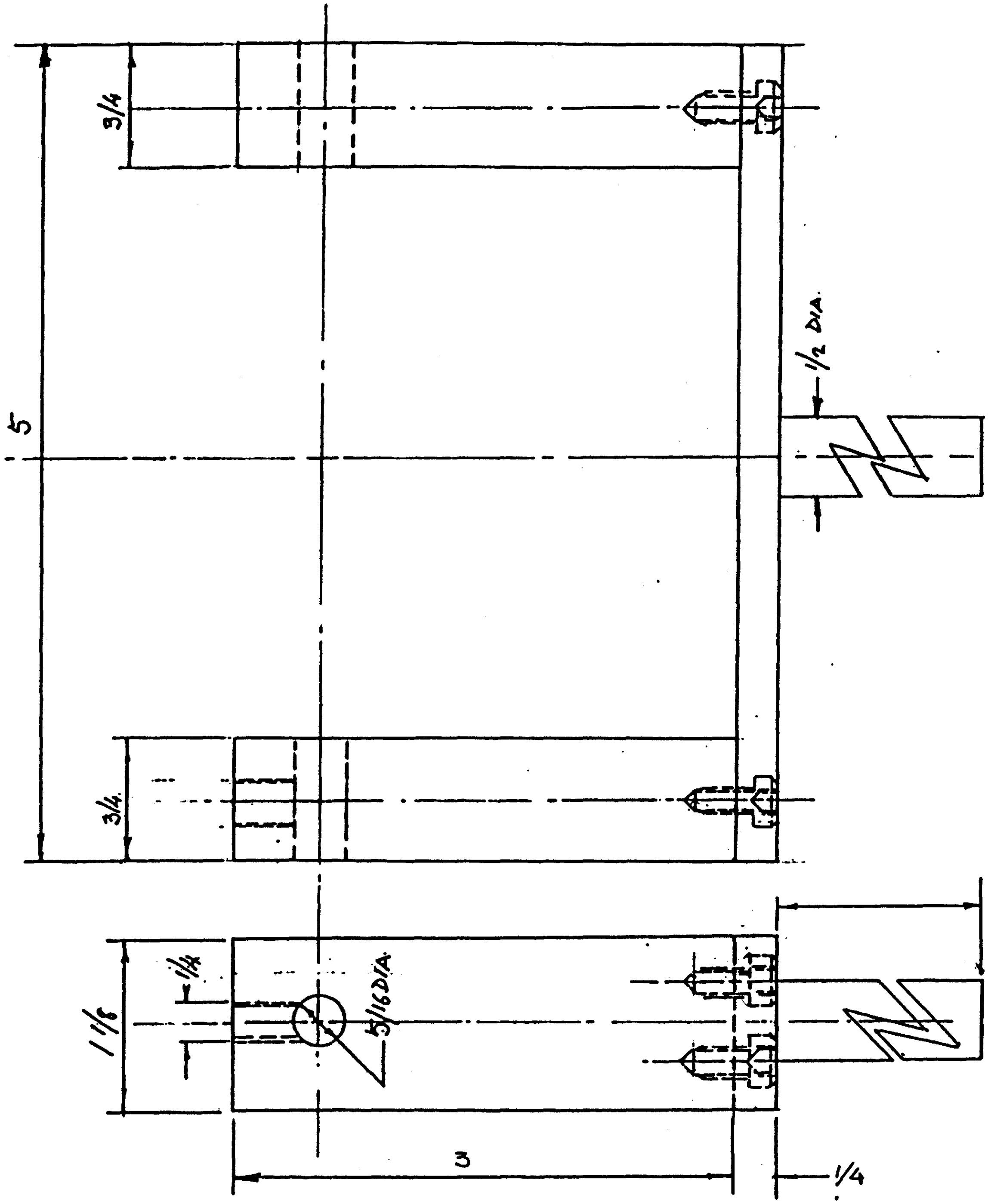

Fig. 4.24 ESA supporting fork.

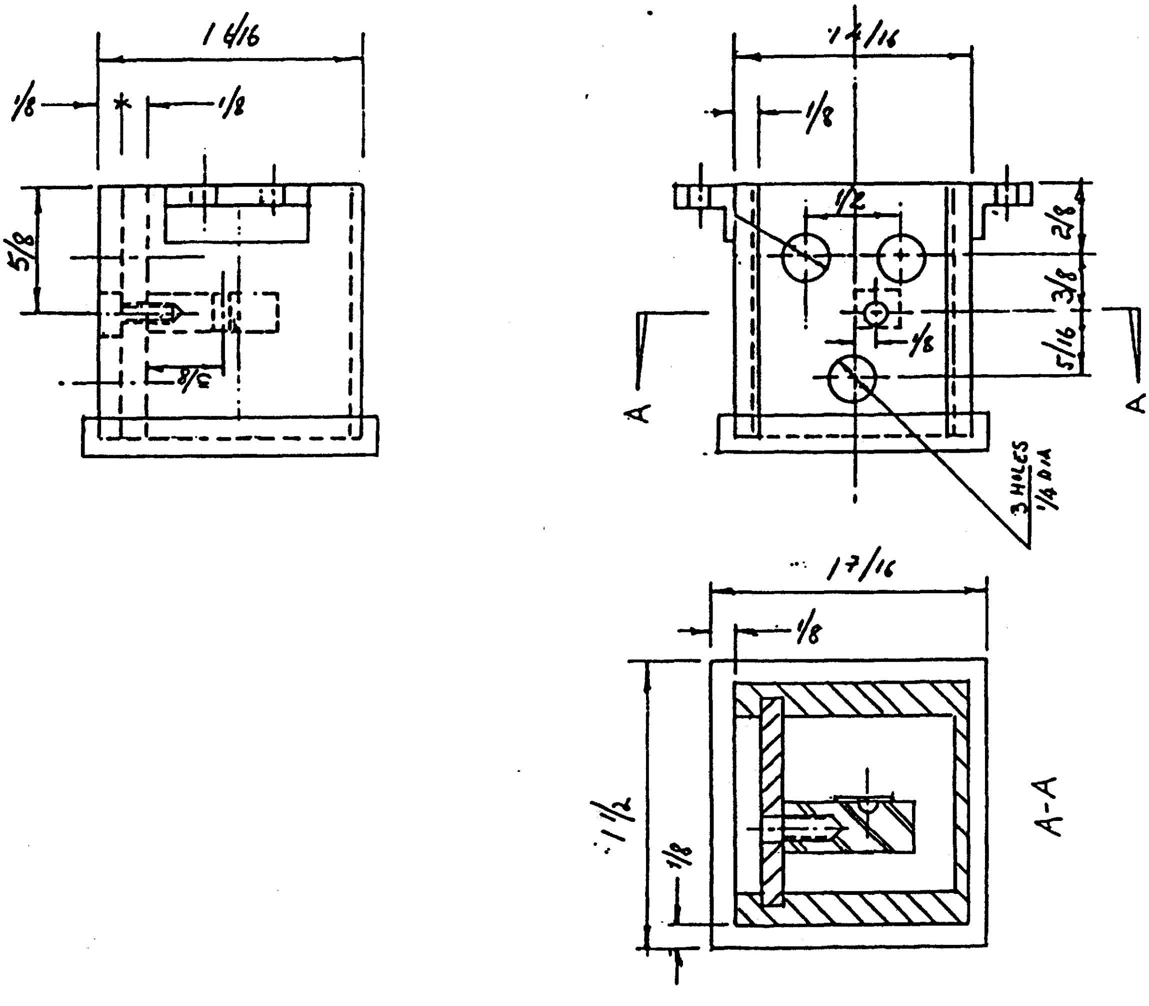

Fig. 4.25 Schematic of the channeltron housing.

transmit the motion from a rotary feedthrough (wobble stick type) to the upper platform. Flexible bellows couple the shaft of the feedthrough to the protruding gear shaft. The fork mount was used for supporting the analyser and channeltron housing (Figure 4.24).

All components had provisions for mechanical alignment at assembly time. The analyser housing could be tilted about the vertical and horizontal axis of the supporting fork and its distance from the flange could be varied. The bottom platform permitted the positioning of the vertical axis of rotation of the top platform. Once all adjustments were completed, set screws were used to tighten the components in place.

Nickel rings mounted on insulator standoffs allowed unimpeded 360^{o} electrical connection with a set of phosphorus bronze spring contacts used for the delivery of biasing voltages to the ESA and channeltron. Nickel wires insulated with ceramic beads connected the rings to electrical feedthroughs at the bottom flange.

4.6 The UHV Chamber

The following is a list of the port requirements for the UHV chamber:

(1) Input ion beam
(2) Time-of-flight arm
(3) Sputter ion gun
(4) Agron gas feed
(5) Electron target heat gun
(6) Auger analyser
(7) Ion pump
(8) Sublimation pump

(9) Roughing pump
(10) Viewing
(11) Quick-load device

4.7 The Data Acquisition System

The objective in the design of the data acquisition system was to provide the capability of scanning automatically the backscattered particles energy spectrum in such a manner so that the dwell time per energy window is dependent on the beam current at the target and also on a manually controlled setting.

Figure 4.26 is a block diagram of the system electronics. A multichannel analyser operated in the multiscaling mode recorded backscattered particles detected by the channeltron. The voltage across the ESA is determined by the power supply amplifying the output of the D/A converter.

The input section comprises of a picoameter connected to the target, a current integrator and a voltage comparator (Figure 4.28).

During an experiment the picometer charged the current integrator which supplied a voltage to the comparator. When this voltage crossed a potentiometer selected reference level, the comparator generated the channel advance pulse which bumped by one both the MCA channel and the D/A register. This pulse also triggered a monostable which reset the integrator and disabled the MCA from counting until the power supply settled to its new value.

Push buttons controlling the value of the D/A register are used to preset the initial energy of an experimental run. The output from the MSB of this register was used to terminate the run on completion of a single scan.

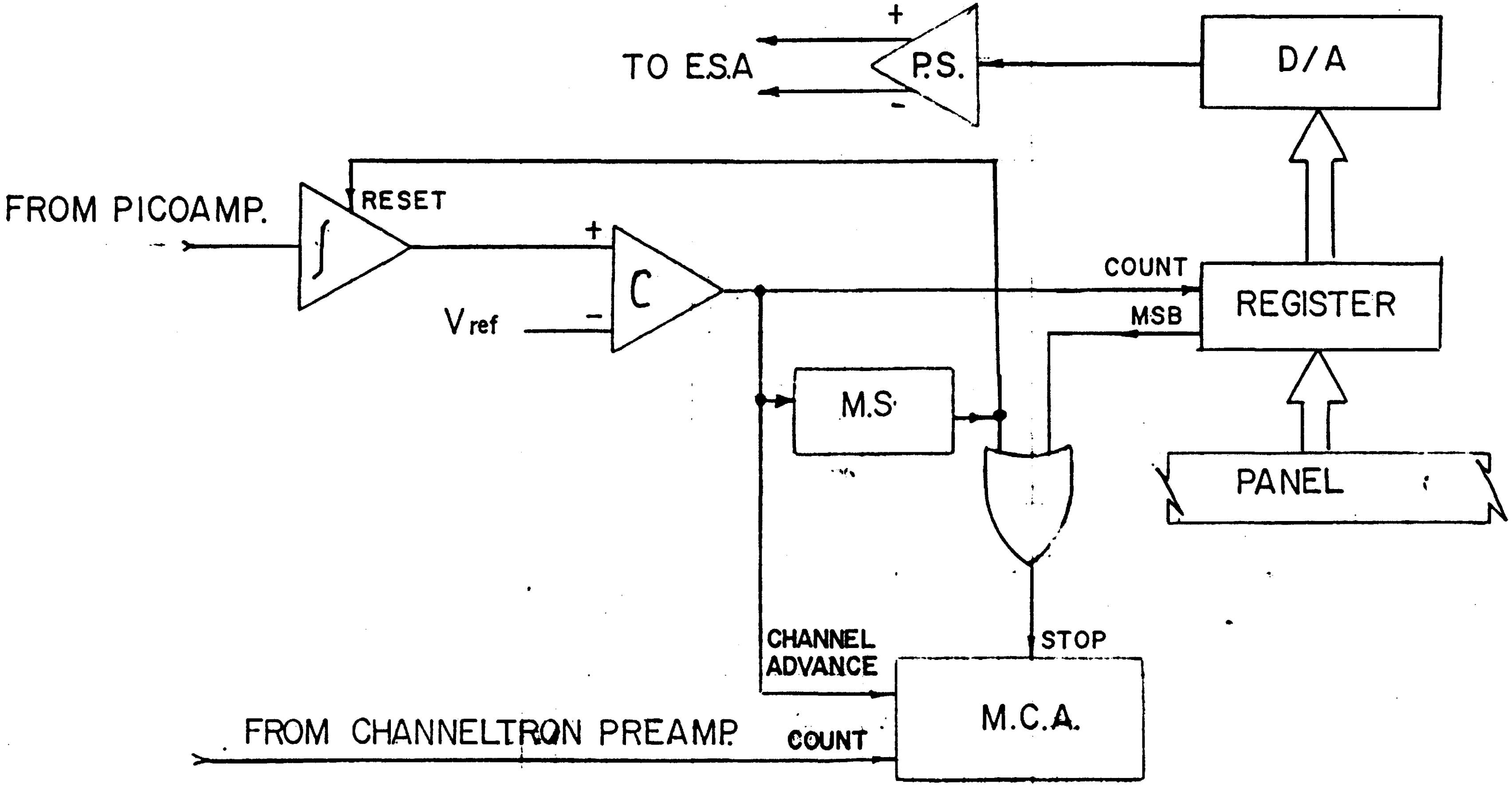

Fig. 4.26 Block diagram of the data acquisition system.

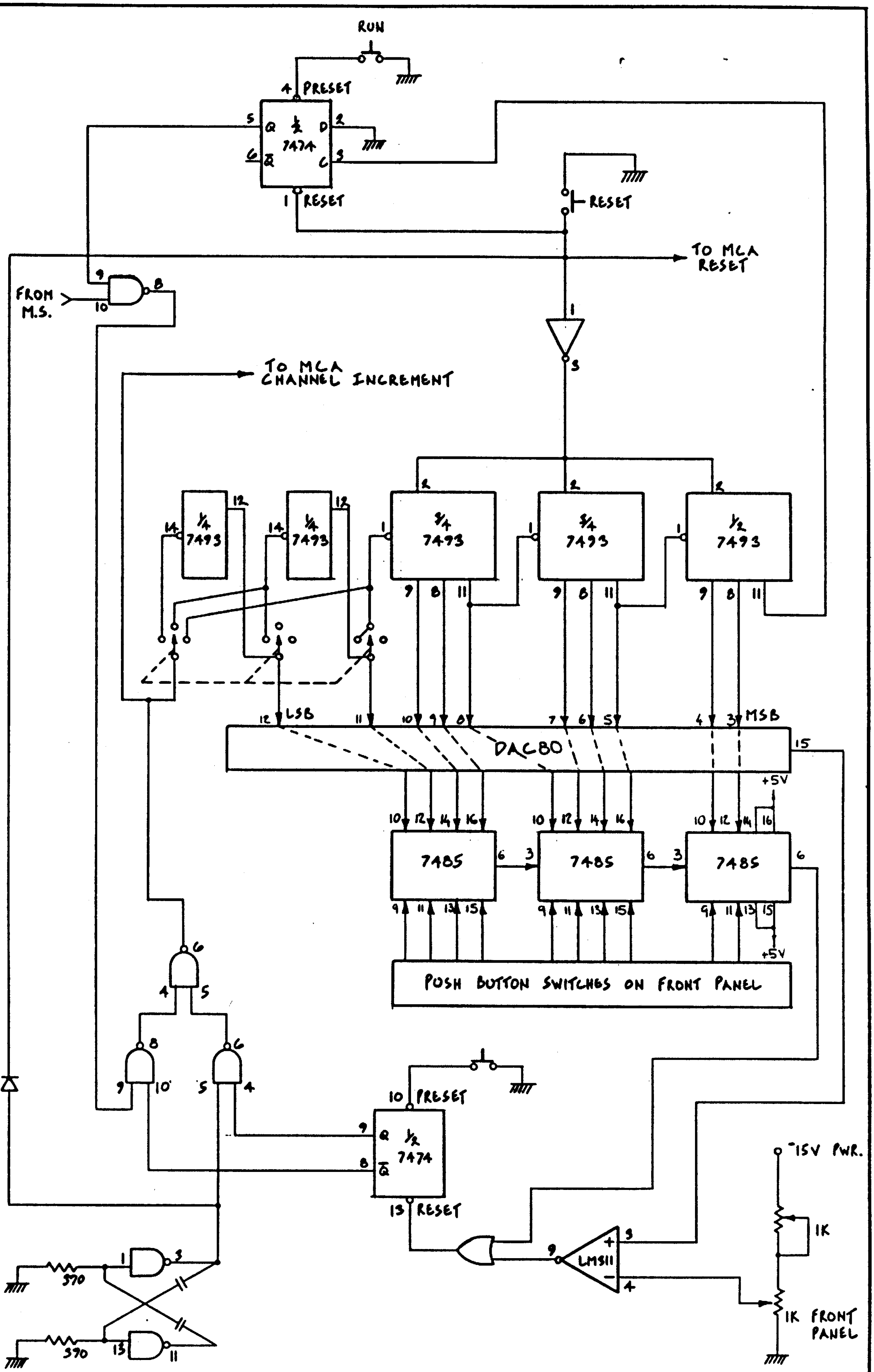

Fig. 4.27 The electronic control system.

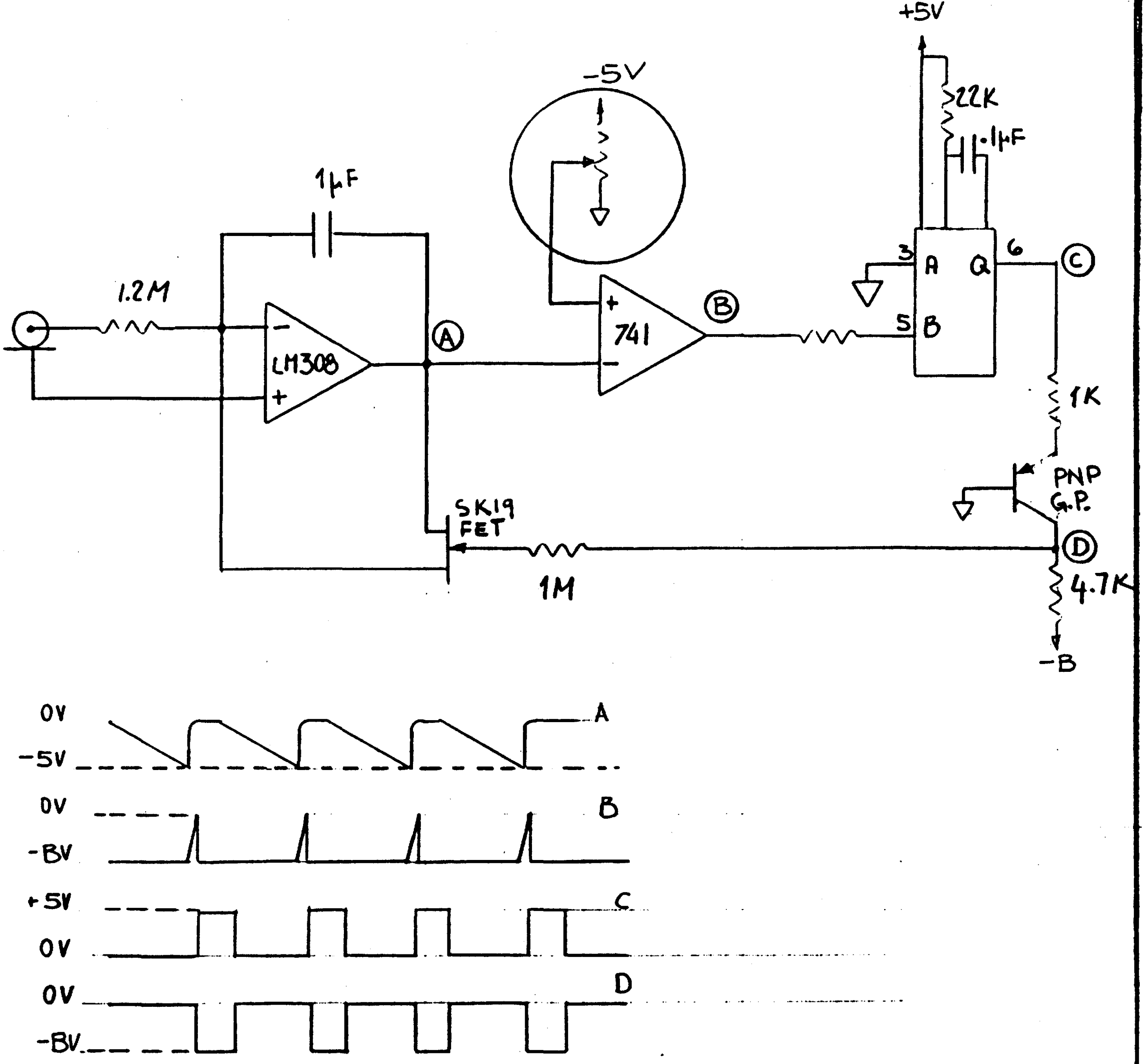

Fig. 4.28 Channel advance pulse generator.

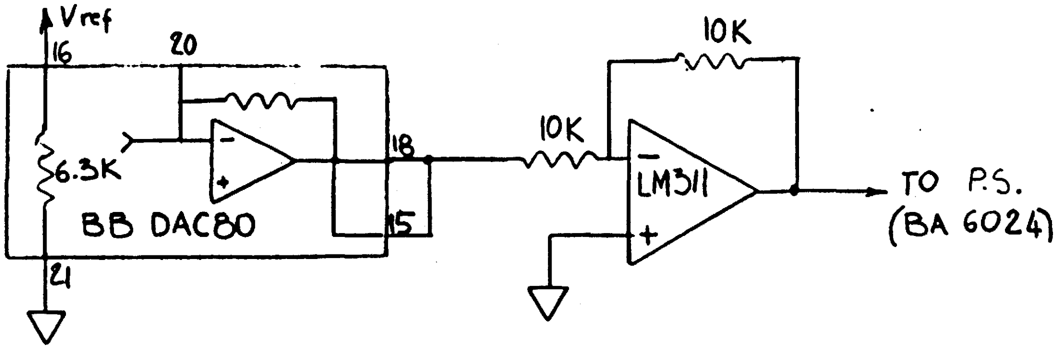

Fig. 4.29 Schematic of the DAC circuit driving the power supply.

The memory contents of the MCA could either be displayed on a X-Y plotter or dumped on a teletype.

4.8 The Energy Analyser and Detector

Figure 4.30 is an assembly drawing of the ESA and channeltron housing. The energy analyser utilized two full hemispheres separated from each other with high precision ground ruby balls. The radius of the beam trajectory is 5cm and the gap between hemispheres is 0.5cm. This device was built at the university of Salford with a special turning attachment, to mechanical tolerances better than ± 0.001".

The focusing and analysing properties of spherical condensers have been discussed by many authors (52,53). The energy resolution is given by eq. 4.1 and is shown to depend on the angular divergence and of the beam, the radius Ro of the optical axis and the width w of the entrance and exit slits. In this case $\Delta E_{½}/E$ was measured to be 1.3%.

$$\frac{\Delta E1/2}{E} = \frac{w}{Ro} - \alpha^{2} \qquad (4.1)$$

The detector (Mullard B312BL) was in the form of glass spiral and had a rectangular section input core of $2.0 \times 8.0\text{mm}^2$. A typical electron gain of such a device biased at 3kv is 1.3×10^6 (54). It's detection efficiency is close to unity for energetic ions but falls off quite rapidly at energies less than 2.7 kev for light positive ions. Consequently, low energy ions must be post accelerated. This can be accomplished by grounding the positive end of the channel electron multiplier power supply thus placing the multiplier input at a high negative voltage.

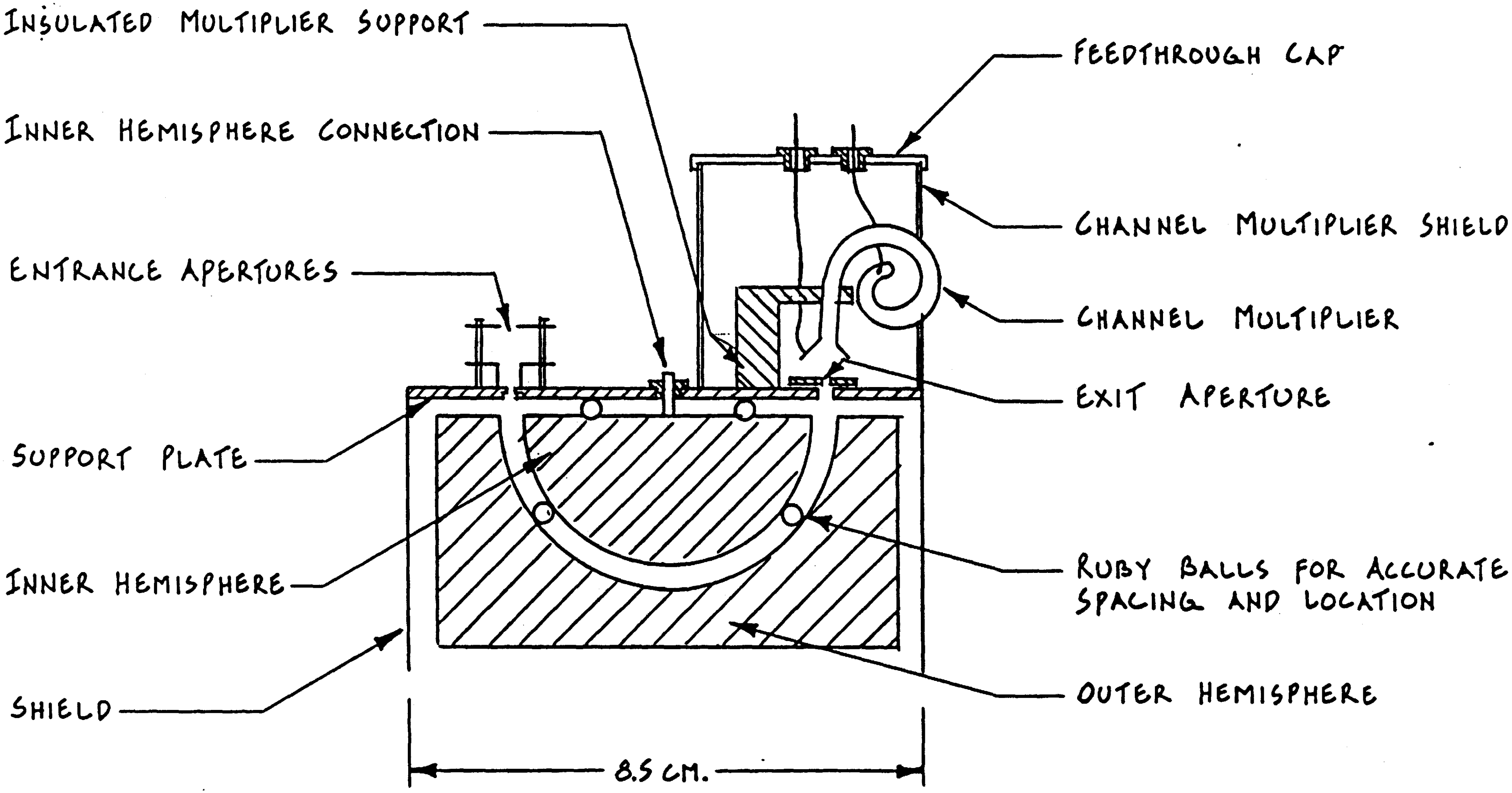

Fig. 4-30 SCHEMATIC ARRANGEMENT OF ELECTROSTATIC ANALYSER

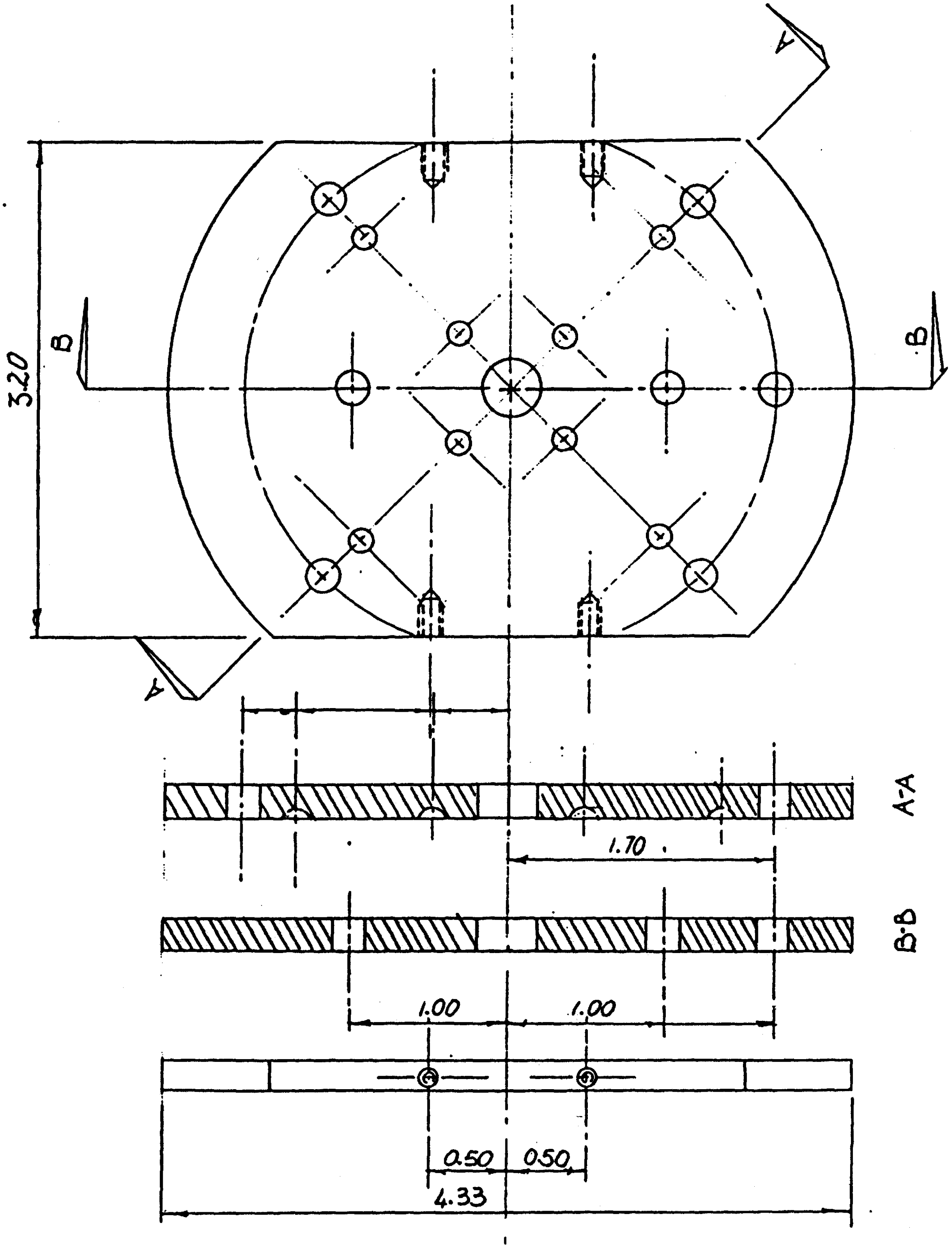

Fig. 4.31 Modifications to the analyser support plate.

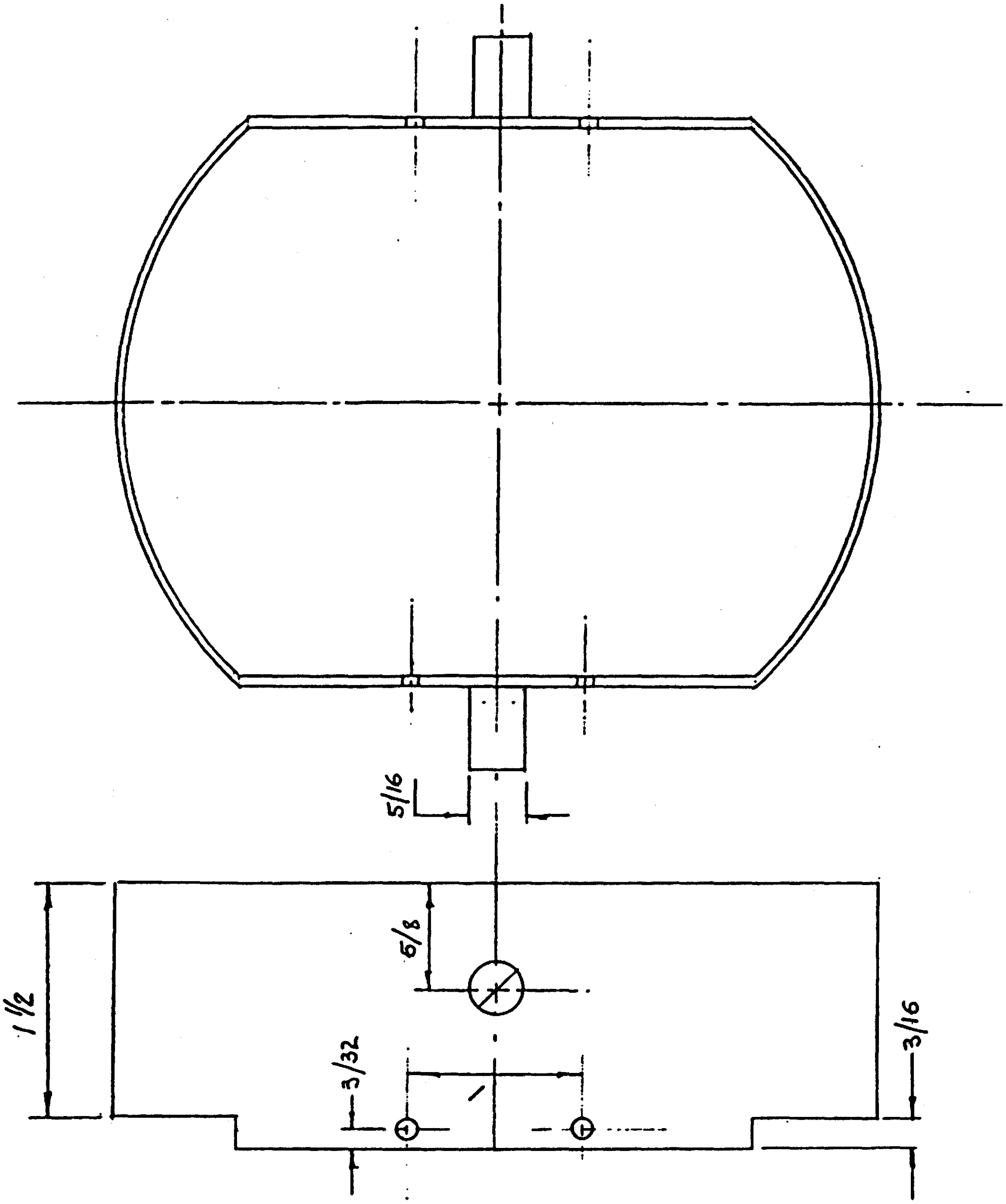

Fig. 4.32 The analyser housing.

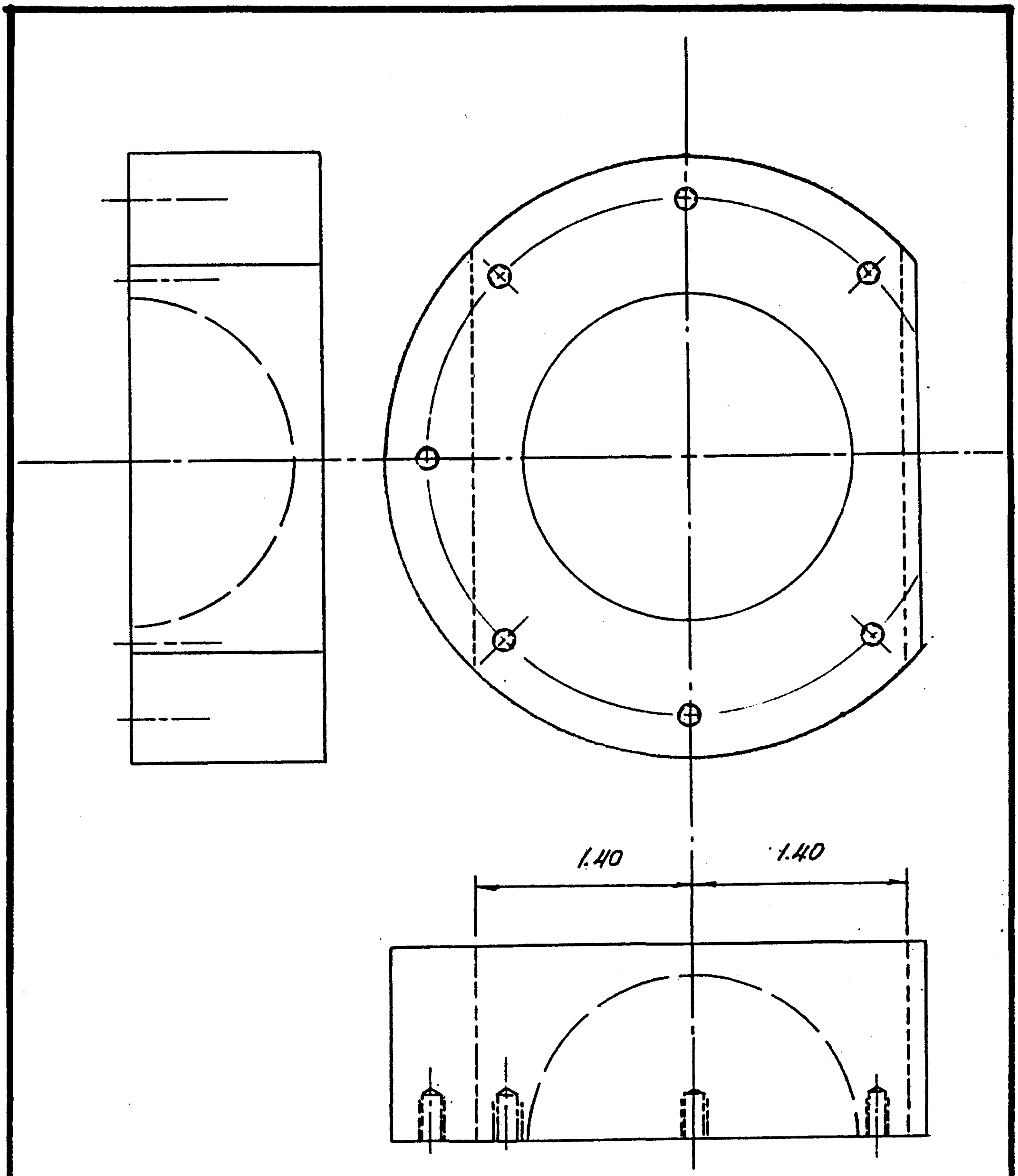

Fig. 4.33 Modifications to the analyser body.

4.9 Evaluation

The proposed mass spectrometer was not tested due to delays on the construction of the various parts. However, some experimental results were obtained by Professor J.E. Robinson.

APPENDIX A

MAGNET DATA

POLES

Each pole-piece is clamped by an Allen screw. When these screws are slackened the pole-pieces may easily be moved to give the required gap, which is adjustable from zero to 1⅞ inches. One end of each pole-piece is plane, and the other end is coned with a half-inch face diameter. It is, therefore, possible to set the gap with either plane or coned pole-tips.

COILS

The coils may be either air-cooled or water-cooled. The mean resistance rise is not to exceed 40% of the cold resistance. This corresponds to maximum continuous currents of approximately:

0.75 amps per coil, air-cooled

1.1 amps per coil, water-cooled

Each coil is wound with 4,900 turns of 24 s.w.g. copper wire, and has a cold resistance of 90 ohms. The hot resistance at the maximum rating is 126 ohms.

With water-cooled operation and the four water-cooling pipes connected in series a flow of 0.22 gal/min (1 litre/min) at 8 lb/in^2 (0.56 kg/cm^2) is needed.

MECHANICAL DATA

Pole diameter 1½ in	Width 9⅞ in
"C" shaped yoke	Front-to-back 5½ in
Height 7$\frac{3}{16}$ in	Weight 42 lb

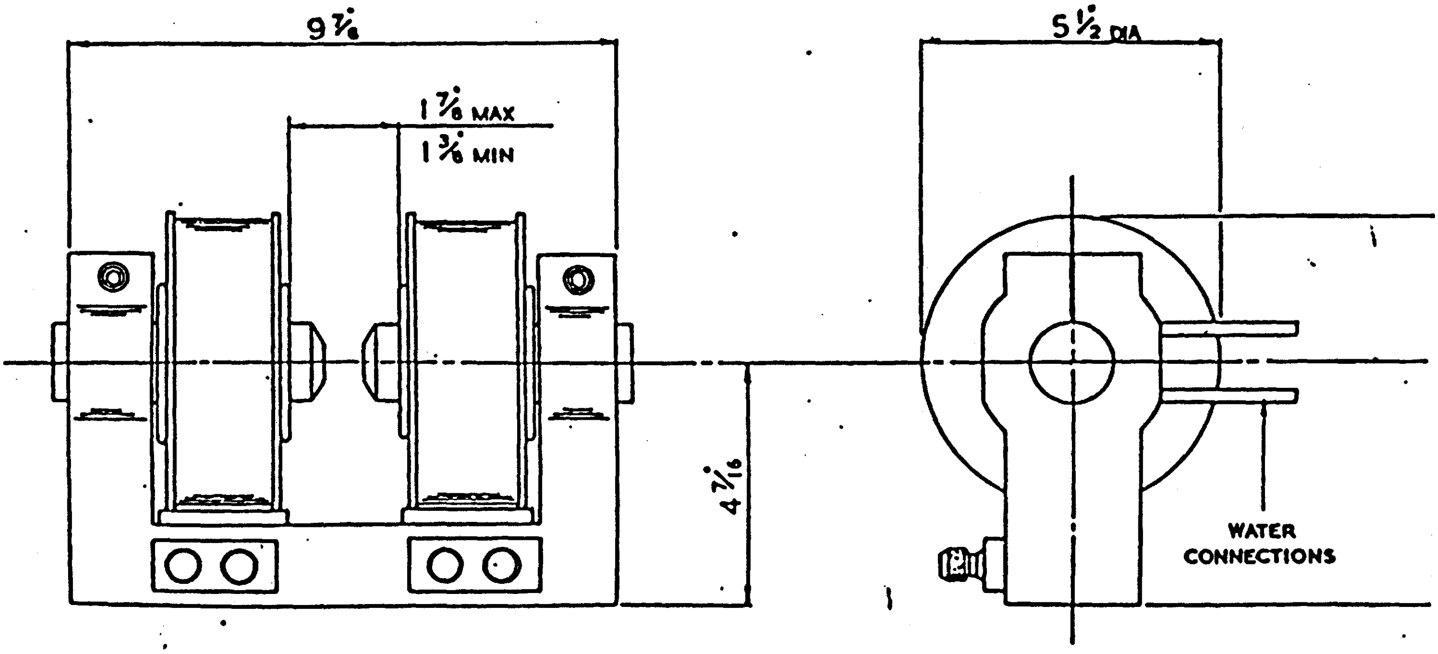

PERFORMANCE CURVES

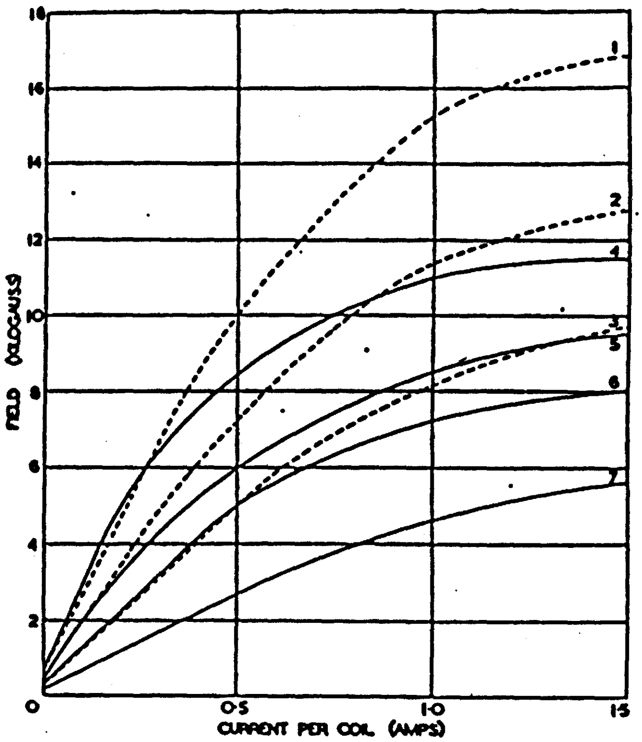

The dotted curves are for ½-inch face diameter coned pole-tips.

The solid curves are for 1½-inch face diameter plane pole-tips.

Curve	Pole Tips	Gap
1	½-in face, 60°	0.5 cm
2	”	0.75 cm
3	”	1.0 cm
4	1½-in face, plane	0.5 cm
5	”	0.75 cm
6	”	1.0 cm
7	”	2.0 cm

If required this magnet can be supplied with axial holes through the poles. It is also possible to replace the plane or coned tips with any other desired profile, for example, that suitable for Faraday susceptibility work.

Power Supply Type VR3 has been designed for use with this magnet (see leaflet PS11a).

REFERENCES

1. 'Report to the American Physical Society by the Study group on Physics Problems relating to Energy Technologies', Rev. Mod. Phys. 47, 529 (1975).

2. Park, R.L. ASTM Special Technical Publication 596, ed. R.S. Carbonara and J.R. Culhill, 3 (1975).

3. Wood, E.A., J. Appl. Phys. 35, No. 4, 1306 (1964).

4. Hagstrum, H.D., Science 178, 275 (1972).

5. Baun, W.L., et al., ASTM Special Technical Publication 596, ed. R.S. Corbonara and J.R. Culhill, 56 (1975).

6. Buck, T.M. et al., Nuclear Instruments and Methods 149, 591 (1978).

7. Firsov, O.B., Soviet Physics Sept. 34, No. 2, 308 (1958).

8. Lindhard, J., Nielsen, V. and Scharff M., Mat. Fys. Medd. Dan. Vid. Selsk. 36, No. 10 (1968).

9. Hagstrum, H.D., Ineleastic Ion-Surface Collisions, ed. N.H. Tolk et al., Academic Pres, New York, pp.1 (1977).

10. Erickson, R.L. and Smith D.P., Phys. Rev. Lett. 34, 297 (1975).

11. Firsov, O.B., Soviet Physics Sept. 36, No. 5, 1076 (1959).

12. Thompson, D.A., Robinson, J.E. and Walker, R., Rad. Effects 32, 169 (1977).

13. Oen, O.S. and Robinson, M.T., Nucl. Instr. Methods 132, 647 (1976).

14. Sigmund, P., Inelastic Ion-Surface Collisions, ed. N.H. Tolk, J.C. Tully, W. Heiland and C.W. White, Academic Press, PP.121 (1977).

15. Gries, W.H., Int. J. Mass Spectr. and Ion Phys. 17, 77 (1975).

16. Sigmund, P., Phys. Rev. 184, No. 2, 383 (1969).

17. Davies, J.A., Corsica Summer School, 29 Aug. - 12 Sept. 1976.

18. Smith, D.P., J. Appl. Phys. 38, No. 1 (1967).

19. Smith, D.P., Surface Science 25, 171 (1971).

20. Ball, D.J., Buck, T.M. MacNair, D. and Wheatley, G., H., Surface Science 30, 69 (1972).

21. Brongersma, H.H., J. Vac. Sci. Technol. 11, No. 1 (1974).

22. Brongersma, H.H. and Buck, T.M., Nucl. Instr. Methods, 149, 569 (1978).

23. Buck, T.M., Chen, Y.S., Wheatley, G.H. and Van Der Weg, W.F., Surface Science 47, 244 (1975).

24. Meischner, P. and Verbeek, H., J. Nucl. Materials 53, 276 (1974).

25. Eckstein, W., Molchanov, V.A., Verbeek, H., 3rd Int. Conf. on Ion Beam Analysis 27.6 - 1.7. 1977, Washington D.C., USA.

26. Rusch, T.W. and Erickson, R.L. Ineleastic Ion-Surface Collisions, ed. N.H. Tolk, J.C. Tully, W. Heiland C.W. White, Academic Press, pp.1 (1977).

27. Eckstein, W. and Verbeek, H., J. Vac. Sci. Tech. 9, 612 (1972).

28. Verbeek, H., Eckstein, W. and Datz, S., J. Appl. Phys. 47, 1785 (1976).

29. Eckstein, W., Matchke, F.E.P. and Verbeek, H., J. Nucl. Materials 63, 199 (1976).

30. Eckstein, W. and Verbeek, H., Vacuum 23, No. 5, 159 (1973).

31. Chen Y.S., Miller, G.L., Robinson, D.A.H., Wheatley, G.H. and Buck, T.M., Surface Science 62, 133 (1977).

32. Buck, T.M. Wheatly, G.H. and Feeldman L.C., Surface Science 35, 345 (1973).

33. Buck, T.M., Wheatly, G.H., Miller G.L., Robinson, D.A.H. and Chen, Y.S., Nucl. Instr. Methods 149, 591 (1978).

34. Andersen, H.H., Lenskjer, T., Sidenious, G. and Sorensen H., (submitted to J. Appl. phys.).

35. McCracken, G.M. and Freeman N.J., J. Phys. B (Atom Molec. Phys.) 2, Ser. 2, 661 (1969).

36. McCracken, G.M., Maple, G.H.C. and Watson H.H., Rev. Sci. Instr. 37, No. 7, (1966).

37. Verbeek, H., J. Appl. Phys. 46, No. 7 (1975).

38. Robinson J.E. and Agamy, S., Atomic Collisions in Solids, ed. by S. Datz, B.R. Appleton and C.O. Moak (Plenum Press, New York), 215 (1975).

39. Robinson, J.E., Harms, A.A. and Karapetsas S.K., Appl. Phys. Lett. 27, No. 8 (1975).

40. Robinson, J.E., Kwok, K.K. and Thompson D.A., Nucl. Instr. Methods 132, 119 (1976).

41. Robinson, J.E., Radiation Effects 23, 29 (1974).

42. Robinson, M.T. and Oen O.S., Phys. Rev. 132, No. 6 2385 (1963).

43. Oen, O.S. and Robinson, M.T., J. Appl. Phys. 35, No. 6 (1964).

44. Inshitani, T., Shimizu, R. and Murata, K., Jap. J. App. Phys. 11, No. 2 125 (1972).

45. Krauss, A.R. and Gruen, D.M., Nucl. Instr. Methods 149, 547 (1978).

46. Agamy, S.A. 'Backscattering of 5-15 KeV Light Ions From Silicon, PH.D. Thesis, McMaster Univ. (1978).

47. Frame, D.J., 'An Optimum Electrostatic Lens Design for a KeV Ion Beam', Undergraduate Project Report, McMaster Univ., Eng. Physics (1973).

48. 'Clean and Ultra High Vacuum Pumping System' Vg Technical Information.

49. 'Ultra High Vacuum Vessel Design' Ug. Technical Information.

50. Halama, H.J., J. Vac. Sci, Tech. 14, No. 1, (1977).

51. Wittan, K.K., 'Development of a Vacuum Transfer System for Tokamak Plasma Impurity Studies', M. Eng. Project Report, McMaster Univ., Eng. Physics (1978).

52. Panin, B.V., Soviet Physics Sept. 15, No. 2, 215 (1962).

53. Purcell, E.M., Phys. Rev. 14, 818 (1938).

54. 'Channel Electron Multipliers', Genelar Explanatory Notes, Mulard (Dec. 1970).

55. Behrisch, R., Eckstein, W., Meischner, F., Scherzer, B.M.U. and Verbeek, H., 3rd Int. Conf. on Atomic Collisions in Solids, Gatlinburg, Sept. 23-28, 1973.

56. Behrisch, R., Muhlbaver, G., and Scherzer, B.M.U., J. Sci. Instr. (Journal of Physics E) 2, 381 (1969).

57. Becker, H., Dietz, E. and Gerhardt, U., Rev. Sci. Instr. 43, No. 11 (1972).

58. Lindhard, J., Scharff, M. and Schiott, H.E., Mat. Fys. Dan. Vid. Selsk. 33,, No. 14 (1963).